Compositional changes in deglacial red mud event beds off the Laurentian Channel reveal source mixing, grain-size partitioning and ice retreat

Wei Leng [a, d, *], Tilo von Dobeneck [a, *], Janna Just [a], Aline Govin [b], Guillaume St-Onge [c], David J.W. Piper [d]

[a] MARUM-Center for Marine Environmental Sciences and Faculty of Geosciences, University of Bremen, Bremen, Germany
[b] LSCE/IPSL, Laboratoire des Sciences Du Climat et de L'Environnement (CEA-CNRS-UVSQ), Université Paris-Saclay, 91190, Gif-Sur-Yvette, France
[c] Institut des Sciences de La Mer de Rimouski (ISMER), Canada Research Chair in Marine Geology, Université Du Québec à Rimouski and GEOTOP, Rimouski, QC, Canada
[d] Natural Resources Canada, Geological Survey of Canada, Bedford Institute of Oceanography, Dartmouth, NS, Canada

ARTICLE INFO

ABSTRACT

Between 22 and 17 cal ka BP, five large meltwater events from within the Laurentian Channel Ice Stream deposited mud beds meters thick across a large area of the Laurentian Fan and adjacent continental slopes. This study determines the sources of these event beds and relates them to the glaciological evolution of the retreating Laurentian Ice Stream. We analyzed major element and magnetic mineral contents of these event beds and compare them with a new collection of 80 source reference samples from the Gulf of St. Lawrence area. Element ratios suggest a steady compositional change from older to younger outburst event beds, while element-specific offsets from reference sample compositions indicate grain-size and mineral/element partitioning during suspension transport. Their magnetic properties place event beds on the source mixing trend of four reference samples groups, which represent two magnetite-rich sources (Canadian Shield and/or Southern Newfoundland) and two hematite-rich sources (Appalachian red beds). Using a deterministic linear source mixing model based on IRM_{100mT}, HIRM and Ca%, we find that the earlier two outburst events had higher contributions from granitic and calcareous sources than the later three events. Combining materials, timing and scenarios of the outburst events with ice-sheet retreat and ice-stream dynamics, we argue that the subglacial sediment depocenter of the earlier two event beds was located in the lower Laurentian Channel while that of the later three events was upstream from Cabot Strait.

© 2019.

1. Introduction

The 1400 km long, 100–150 km wide and 300–550 m deep Laurentian Channel trough (Fig. 1) that winds from the St. Lawrence Estuary past Anticosti Island through the shallow basins of the Gulf of St. Lawrence to the edge of the Grand Banks Shelf, is among Canada's most remarkable bathymetric features. It was originally shaped by a Neogene fluvial system that was later occupied by the Laurentian Channel Ice Stream (LCIS) draining in a southeasterly direction into the NW Atlantic (Fig. 1). During the last (Wisconsinan) glaciation, the LCIS was active from at least ~22 until ~16.5 ka (Shaw, 2002; Shaw et al., 2006; Margold et al., 2018). During this period, the ice sheet margins retreated in large steps from a shelf edge position first to Cabot Strait and finally up the main and side branches of the LCIS, turning the ice-covered Gulf of St. Lawrence into an open-water calving bay (Josenhans and Lehman, 1999; Piper and Macdonald, 2001). It can be assumed that the thinning of the ice stream may initially have formed isolated subglacial meltwater lakes, followed by subglacial intrusion and later proglacial invasion of sea-water. Unconsolidated glaciomarine mud deposits in the channel bed (King, 2014) are evidence of such past conditions, and these deposits may have been episodically reworked and partly exported by vigorous subglacial outburst floods (Piper et al., 2007, 2012), dispersing large quantities of fine reddish sediment over the adjacent Scotian and Newfoundland continental slopes and the Sohm Abyssal Plain (Skene and Piper, 2003). By analyzing four matching sediment records of this "reddish plumite" sequence retrieved from the SW Grand Banks Slope of Newfoundland, Leng et al. (2018) identified five subsequent Laurentian outburst flood event units with ages of ~22.0, 21.6, 19.5, 18.1 and 17.9 ka.

These "red plume" deposits were initially thought to originate mainly from Permo-Carboniferous Appalachian red bed formations (Needham et al., 1969; Alam and Piper, 1977) extending from New Brunswick over the southern and central parts of the Gulf of St. Lawrence (Fig. 1). The rock-magnetic data of Leng et al. (2018) show, however, that the stacked plumite beds gradually evolve from a more magnetite-dominated (e.g. granitic) to a more hematite-dominated (i.e. sedimentary) magnetic mineralogy; their data also give hints of a third, low-magnetic, and possibly calcareous source. These progressive compositional changes in the plumite beds suggest that various source areas in the LCIS catchment contributed to changing proportions of the glaciomarine channel-bed deposits of the past deglacial period. While these channel-bed deposits were repeatedly

* Corresponding authors. MARUM-Center for Marine Environmental Sciences and Faculty of Geosciences, University of Bremen, Bremen. Germany.

Email addresses: weileng@uni-bremen.de (W. Leng); weileng@uni-bremen.de (T. von Dobeneck)
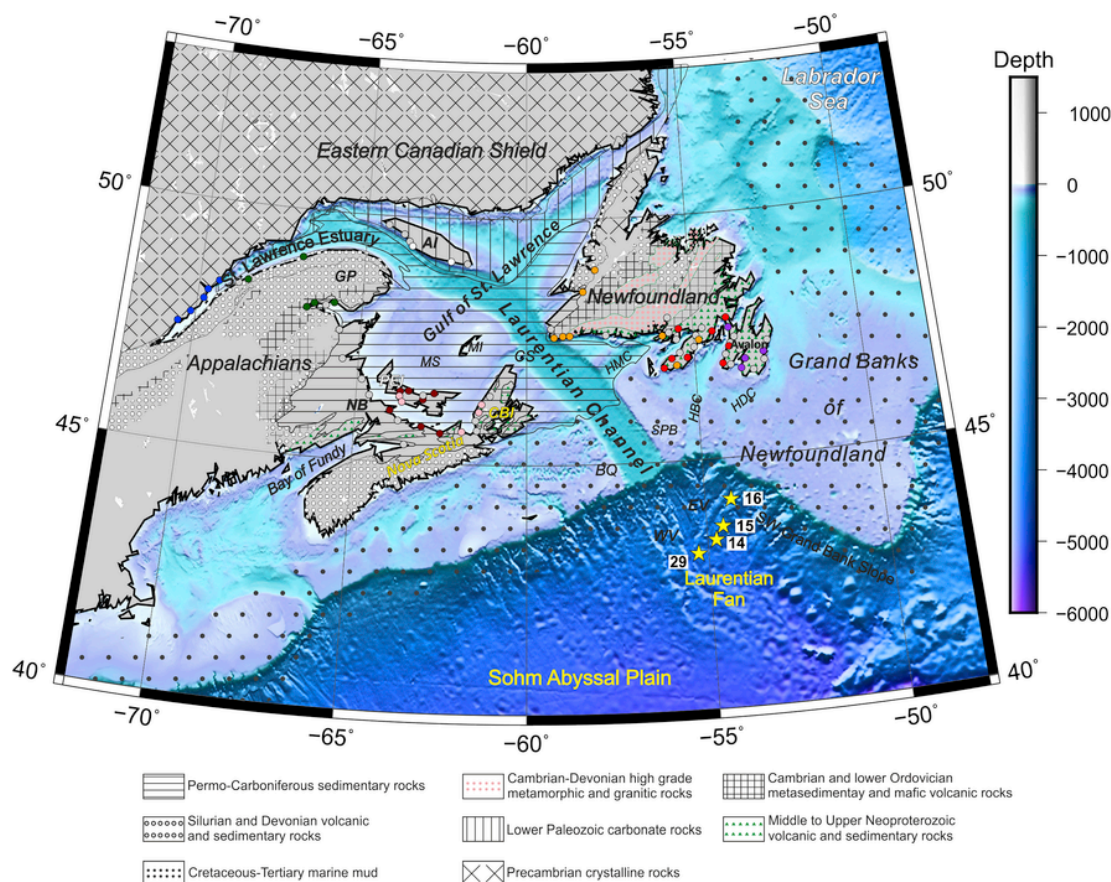
Fig. 1. Geological and bathymetric map of eastern Canada and Gulf of St. Lawrence. Yellow stars show locations of gravity cores 14 (GeoB18514-2), 15 (GeoB18515-1), 16 (GeoB18516-2) and 29 (MD95-2029) on the SW Grand Banks Slope. Dots mark the locations of coastal and estuary reference samples from the Gulf of St. Lawrence and Newfoundland; their different colors represent the groupings (Table 1, Table S1 in Supplement) discussed in Chapt. 4.2. Regional patterns denote bedrock geology units with simplified boundaries from Williams and Grant (1998). AI=Anticosti Island, CBI=Cape Breton Island, BQ=Banquereau, CS=Cabot Strait, EV=Eastern Valley, GP=Gaspé Peninsula, HBC=Halibut Channel, HDC=Haddock Channel, HMC=Hermitage Channel, MI=Magdalen Islands, MS=Magdalen Shelf, NB= New Brunswick, PEI=Prince Edward Island, SPB= St. Pierre Bank, WV= Western Valley. (For interpretation of the references to color in this figure legend, the reader is referred to the Web version of this article.)

washed out, their compositions remain archived in the plumite successions around the Laurentian Fan system.

(Semi-) quantitative sediment source identification of glaciogenic marine sediments, with or without source reference data, is a key method to reconstruct past ice sheet dynamics and sedimentation in the Northwest Atlantic, Labrador Sea and Baffin Bay. Past sediment provenance studies have used different markers for source characterization, e.g. major minerals (Simon et al., 2014; Casse et al., 2017), heavy minerals (Tsikouras et al., 2011), major elements (Pe-Piper et al., 2008; Just et al., 2012a, 2014), magnetic minerals (Stoner et al., 1996, 1999; Just et al., 2012b; Hatfield et al., 2013, 2016; 2017; Razik et al., 2015) and physical properties (Roger et al., 2013). All these approaches work well under favorable circumstances (Hemming, 2004), but also encounter problems like non-uniqueness, unknown distal sources, source heterogeneity, weathering and transport partitioning (Weltje, 2012; Heslop, 2015). The term transport partitioning encompasses compositional changes (e.g. grain size, grain shape, mineralogy) that suspended sediments experience during hydraulic and gravitational fractionation, abrasion, and weathering along the transport path. Sediment unmixing models provide most robust results when singular or very prominent compositional features of potential sources are included, permitting their identification as even minor constituents of complex mixtures.

The typical bedrock types of the Gulf of St. Lawrence region exhibit contrasting contents of hematite, magnetite (Leng et al., 2018)

and calcite/dolomite (Loring and Nota, 1973), which is why a combination of rock-magnetic and geochemical fingerprinting methods is favorable. The rapidly accumulating plumites from subglacial outburst floods were not significantly diluted by marine background sedimentation and their source characteristics are probably well preserved as they are not bioturbated.

Following the source-sampling concept of Hatfield et al. (2017), we collected 80 estuarine and coastal reference samples along accessible shorelines of the Gulf of St. Lawrence (Fig. 1) with the objective of representing all major source rock lithologies. New major element data of the previously studied plumite sequences (Leng et al., 2018) and analogous rock-magnetic and geochemical data of all reference samples permit us now to set up a linear source end-member mixing model. Our analytical approach also combines compositional data with new grain-size information in the perspective to:

1. Better specify the geological provenance of the Laurentian outburst flood deposits;
2. Outline areas of major bedrock erosion over the active phase (~22–16.5 ka) of the LCIS;
3. Delineate grain-size and mineral fractionation processes during channel-bed erosion and hyperpycnal plume dispersal;
4. Identify subglacial sediment depocenters under retreating ice margin conditions;

5. Examine the ability of deterministic end-member mixing models based on mineral-selective rock-magnetic and geochemical data to uncover such interlinked sediment transport processes.

2. Geological setting

2.1. Geology of the Gulf of St. Lawrence area

The Gulf of St. Lawrence (the Gulf) is a 226,000 km² large triangular marine inlet bordered by Nova Scotia in the south, the Appalachians of New Brunswick and Quebec in the west, the eastern Canadian Shield in the north, and the Newfoundland Appalachians in the east (Fig. 1). The preglacial lowland morphology of the Gulf was further eroded by Pleistocene glaciations. Its surficial sediments are mostly relicts from ice advances and retreats since the late Wisconsinan maximum, modified by postglacial marine high-stand sediment deposition and redistribution (Loring and Nota, 1973). As the modern marine estuary of the St. Lawrence River and past catchment of the LCIS, the Gulf has been a source area as well as a temporary depocenter for sediments ultimately deposited on Laurentian Fan.

The relict sand and gravel beds of the Gulf of St. Lawrence typically show regionally varying mixed compositions of sandstones, crystalline rocks and limestones (Loring and Nota, 1973) reflecting the four main rock categories in the LCIS catchment (Fig. 1). Reddish Upper Paleozoic (Permo-Carboniferous) Appalachian sandstones and siltstones form the bedrock of Nova Scotia, New Brunswick, Prince Edward Island and NE Newfoundland inner shelf and underlie the central and southern Gulf. The northern parts of the Gulf including Anticosti Island consist of grey Lower Paleozoic (Ordovician-Silurian) carbonate rocks of the former Appalachian Foreland. Gaspé Peninsula and the southern bank of St. Lawrence Estuary, as well as the southwest Nova Scotia and small parts of NE Newfoundland are mainly composed of clastic sedimentary rocks of Late Neoproterozoic to Silurian ages. The steep northern coast of the Gulf is the border of the Canadian Shield, which is made of crystalline igneous and metamorphic Precambrian rocks such as granites, granodiorites, gneisses, and schists.

The Laurentian Channel trough links the Gulf via Cabot Strait to the Scotian and Grand Banks shelves. Pleistocene ice stream advances have plastered the channel with up to 18 aggradational layers of glacial till (King, 2014). These clastic sediments facilitated and focused rapid flow of the ice stream by reducing glacial bed shear stress (e.g. Alley et al., 1986). During the last deglaciation, glaciomarine Downing Silt and later postglacial Placentia Clay draped the channel trough and other smaller depressions of the Gulf (Syvitski and Praeg, 1989; King, 2012). Progradational mass transport from the front of the LCIS formed the Laurentian Fan system that channels gravitational sediment transport from the outer shelf through a system of slope valleys into the Sohm Abyssal Plain.

The Scotian Shelf and the Grand Banks of Newfoundland are built of siliciclastic and calcareous sediments of Mesozoic and Tertiary age deposited during the opening of the North Atlantic (Wheeler et al., 1996). In the Quaternary, the sediments of the Grand Banks area were mainly sourced from the glaciated Newfoundland terrane complex, delivered by ice-streams along Hermitage Channel, Halibut Channel and Haddock Channel (Batterson et al., 2006). Granitic and metamorphic materials of Cambrian to Devonian age were eroded from the central Newfoundland Gander Zone while Neoproterozoic siliciclastic and volcanic materials originated from the eastern Newfoundland Avalon Zone (Wheeler et al., 1996).

2.2. Major element distribution and partitioning in Gulf of St. Lawrence sediments

In their comprehensive geological study of the entire Gulf of St. Lawrence, Loring and Nota (1973) presented detailed major element distribution maps and diagrams for sands and silts delineating regional characteristics and contrasts, some of which we digitized and briefly review here because of their high specific relevance for our study. Geochemical analyses of 18 area-representative sieve-fractionated samples quantify the impact of grain-size partitioning on element concentrations and ratios (Fig. 2) highlighting the necessity to
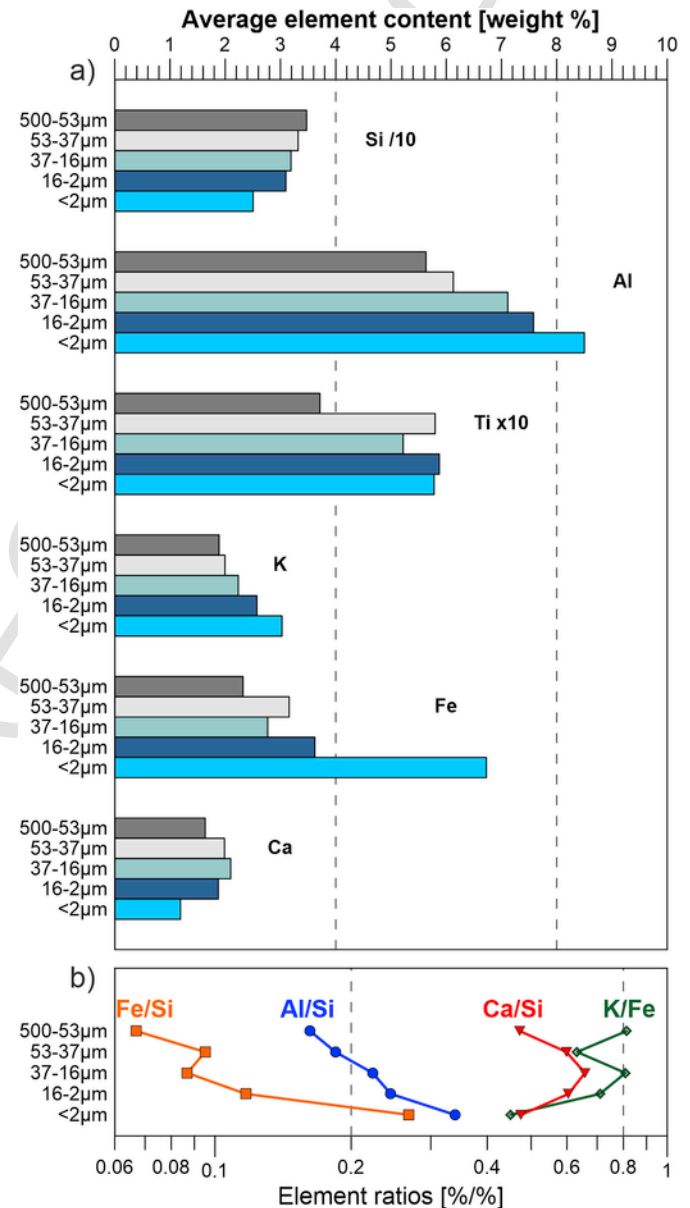
Fig. 2. (a) Average elemental contents of the various grain-size grades in the detrital fractions of 18 sediment samples collected over the entire Gulf of St. Lawrence (Loring and Nota, 1973). Note that Si data were divided by 10 (/10) and Ti data multiplied by 10 (x10) to be plotted on a common abscissa with all other data. **(b)** Variation of major element ratios with grain-size grades in the detrital fractions using the values of (a).

consider the partitioning bias in provenance studies. According to Loring and Nota (1973), all of the surface sediments in the Gulf of St. Lawrence are predominantly of detrital origin since biogenic production was absent or negligible during the Wisconsinan and remained low in the Holocene. The observed element distributions should therefore largely mirror the bedrock of the shelf areas and hinterland of the modern Gulf.

The element distribution maps of Loring and Nota (1973) also help identifying the source-specificity of major element contents, which is fundamental to our study. The major element Si is sourced from all siliceous rocks and sandstones. Its concentration varies little between 25 and 30 wt% except for the southwestern part of the Gulf, the Magdalen Shelf, where the Appalachian formations let Si contents rise up to 42 wt%. Si content slightly decreases with decreasing grain-size since quartz grains are generally large (Fig. 2a). Al content varies from 2 to 9 wt%; it is lower (2–5 wt%) in the Southern Gulf and higher (6–8 wt%) in the Northern Gulf along the Canadian Shield, whose magmatic rocks contain aluminosilicates such as feldspars, micas and clays. Al content shows moderate grain-size dependence being enriched in the fine fraction (Fig. 2a). These inverse grain-size dependences of Al and Si reduce the averaged Al/Si ratio (Fig. 2b) from 0.34 to 0.16 over the grain-size range from 2 μm to 500 μm. The most heterogeneously distributed major element of the Gulf is Ca, which has mainly detrital origin and originates almost exclusively from the Paleozoic limestone formations around Anticosti Island (Fig. 1). Detrital Ca contents are below 1 wt% in the Southern Gulf, 2–4 wt% in the Laurentian Channel and on the Northern Shelf and 5–25 wt% in the sector around Anticosti Island. Sand and clay fractions have relatively similar Ca proportions (Fig. 2a). The Ca/Si ratio (Fig. 2b) is ∼0.47 in both sand and clay only slightly increases (0.59–0.65) in the silt fraction, making Ca the most grain-size independent and region-specific major element in the Gulf.

Sedimentary K content varies only slightly with concentrations of 1–2 wt% in the Southern Gulf and around Anticosti Island and 2–2.7 wt% in the Laurentian Channel and Northern Gulf. The distribution pattern of Fe is similar, but more pronounced: Fe contents are 1–3 wt% in the Southern Gulf and Anticosti Island region and 3–5 wt% in the Laurentian Channel and Northern Gulf. Both elements K and Fe are preferentially associated with fine grain sizes, Fe even more than K (Fig. 2b). Ti content shows a lesser grain-size bias and also a less diversified distribution compared to Fe and K with 0.3–0.4 wt% over nearly the entire Gulf, with slightly higher concentrations of 0.5–0.7 wt% at some Northern Shelf locations and lower values around 0.2 wt% in the Magdalen Islands area. Since Fe shows the highest grain-size dependency compared to K, Ti, and Ca, particularly for the clay fraction, all Fe-based element ratios are relatively stable in the sand and silt range, but deviate strongly in the clay fraction (Fig. 2b).

2.3. Sedimentary records of LCIS subglacial outburst events

Alam and Piper (1977) and Skene and Piper (2003) first recognized that the reddish-brown plumite layers deposited on the levees of the Laurentian Fan valleys were formed by multiple outburst floods of the LCIS. Based on a stratigraphic synopsis of one previously published and three new SW Grand Banks Slope records, Leng et al. (2018) established a detailed outburst event stratigraphy. They identified and dated five independent outburst events, named Oa1/Oa2, Ob and Oc1/Oc2, between Heinrich events H1 (17–16 ka; Gil et al., 2015) and H2 (23.5 ka; Stokes et al., 2015) (Fig. 3). The boundaries of these event beds and their hemipelagic interlayers can be easily identified by sediment color, high-resolution rock magnetics and

grain-size (Leng et al., 2018). The sedimentation events created hyperpycnal suspension plumes with typical grain-size ranges of 3–30 μm (mode 6 μm) associated with coarser, probably ice-rafted detritus (IRD) (Leng et al., 2018).

Leng et al. (2018) also inferred from the high homogeneity of the plumite beds that these sediments were not released from various meltwater source regions but instead eroded from pre-mixed glaciomarine channel-bed deposits. They proposed three alternative event scenarios for the hyperpycnal plumes: (1) a meltwater surge into a proglacial lake in the Gulf of St. Lawrence, (2) expulsion of a subglacial lake by back-stopping and bulging of the LCIS, and (3) a subglacial meltwater-injection into a subglacial lake in the Laurentian Channel, e.g. by breaching of an upstream moraine. Not every event necessarily had the same outflow regime, and the preceding channel-bed deposition may have accumulated different sources and grain sizes of glaciomarine sediments along with changing deglacial ice and sub-ice conditions. These open questions are subject of this study and of further ongoing research.

## 3. Materials and methods

3.1. Materials

The three gravity cores GeoB18514-2 (43°22.14′N 54°45.68′W, 4017 m water-depth, 9.26 m length), GeoB18515-1 (43°38.01'N 54°32.90′W, 3628 m water-depth, 10.95 m length) and GeoB18516-2 (44°09.65′N 54°16.32′W, 2505 m water-depth, 9.23 m length) were retrieved during RV Maria S. Merian cruise MSM39 (Mulitza et al., 2015). Hereafter, these cores are referred to as cores 14, 15 and 16, respectively. Their physical and rock-magnetic property logs and ^{14}C dates were published by Leng et al. (2018). Here we present new major element data acquired at 1 cm resolution using an X-ray Fluorescence (XRF) Core Scanner. For calibration purposes, 20 syringe samples were collected from intervals of contrasting composition of all cores and analyzed by energy-dispersive powder X-Ray Fluorescence (EDP-XRF) analysis. 20 cube samples of 6.2 cm³ were selected from five event beds and interlayers of core 14 for grain-size analysis by laser diffraction.

We adapted the source sampling strategy of Hatfield et al. (2017) by collecting modern analogues of potential source materials for the LCIS channel bed sediments (the presumed source of the plumites) at 76 different coastal and estuarine locations in the Gulf of Lawrence and Newfoundland (Fig. 1). In order to obtain samples that are representative of the prevalent source rock types, we collected coastal and estuary sediment samples with varying grain size from typical water depths 0–50 cm (depending on the tidal situation). We looked primarily for sheltered bay sites enabling deposition of mixed sands, silts or muds and did not sample close to rocky shores, open beaches and organic-rich muds. All samples were wet-sieved through a 1 mm sieve to remove larger organisms. This sediment was filled into 6.2 cm³ non-magnetic cubes and analyzed with various rock magnetic methods. These samples were subsequently freeze-dried and pulverized for EDP-XRF powder analysis. We also include four previously collected carbonate rock samples from Anticosti Island, which were investigated by identical rock magnetic and EDP-XRF powder analyses.

3.2. Methods

3.2.1. Grain-size analyses

Particle-size measurements were performed at MARUM with a *Beckman Coulter Laser Diffraction Particle Size Analyzer LS 13320*.
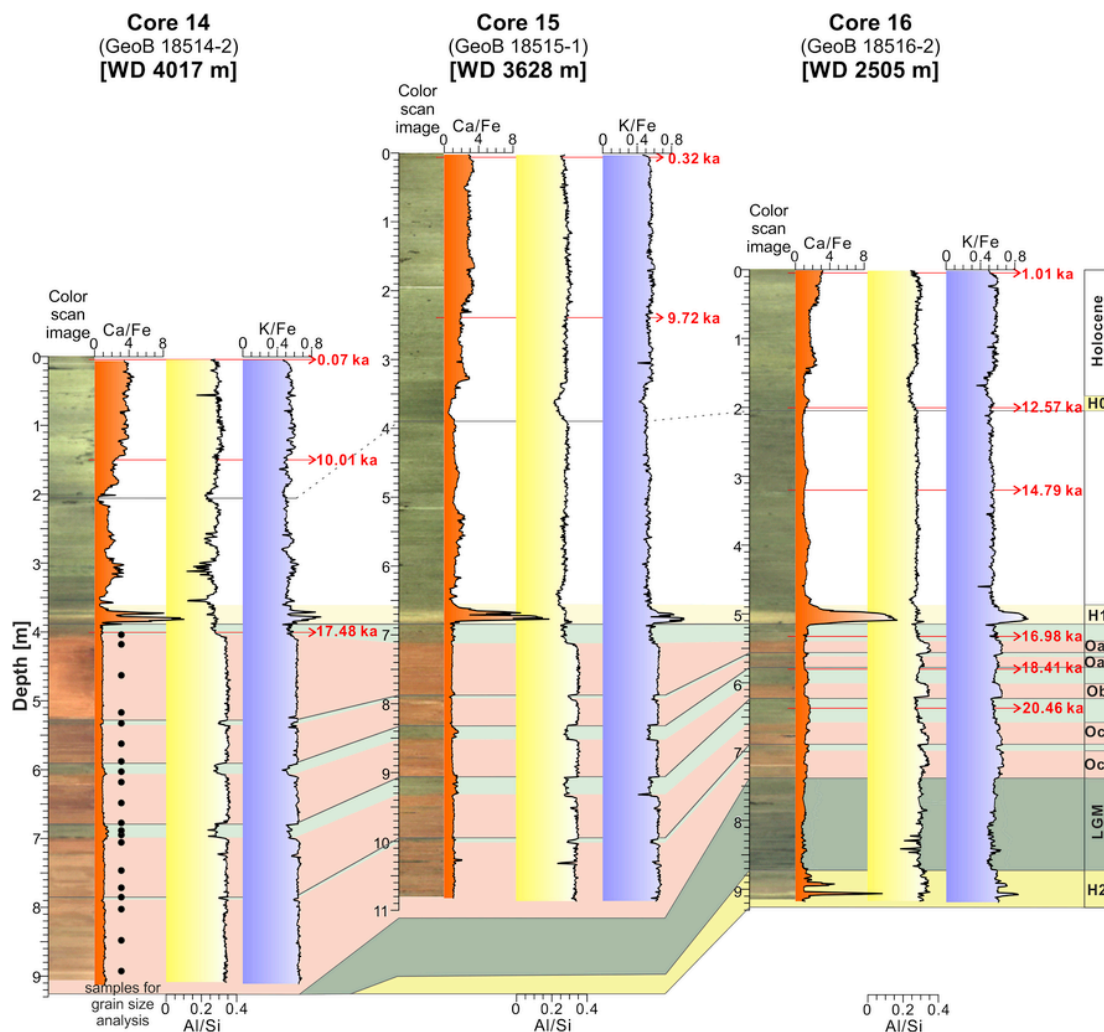
Fig. 3. Stratigraphy of cores 14, 15 and 16 with major element ratio (Ca/Fe, Al/Si and K/Fe) logs. Stratigraphic compilation of contrast-enhanced color scan images and ^{14}C dates (red arrows) shown as calibrated calendar ages from Leng et al. (2018). WD = water depth. Stratigraphic correlation is shown by colored bars, yellow for Heinrich layers H0 (Younger Dryas), H1 and H2, red for reddish-brown event layers Oa1-Oc2, light green for their hemipelagic interlayers and dark green for the Last Glacial Maximum (LGM). Samples of core14 selected for the grain-size analysis are marked by black dots. (For interpretation of the references to color in this figure legend, the reader is referred to the Web version of this article.)

Prior to the measurements, the terrigenous sediment fractions were isolated by boiling the samples with H_2O_2, HCl and NaOH, removing organic carbon, carbonate, and biogenic opal. Particle-size spectra were obtained for 116 size classes from 0.04 to 2000 μm.

3.2.2. Major element analyses

Major element intensities of Al, Ca, Fe, K, Si and Ti were analyzed every 1 cm on the archive halves of cores 14, 15 and 16 with the MARUM *AVAATECH* XRF Core Scanner II using an *Oxford Instruments 50W XTF5011* X-Ray tube with rhodium (Rh) target material at 10 kV. To calibrate the scanner-based elemental intensities, 15 bulk sediment samples from different stratigraphic units of the three cores were freeze dried, powdered and analyzed by energy dispersive polarization X-ray fluorescence (EDP-XRF) spectroscopy at MARUM. We applied the log-ratio approach (Weltje and Tjallingii, 2008) to calibrate scanner XRF intensities to element concentrations from powder analyses. The calibration takes Ca as denominator element to get the calibrated proportions of six elements (Ca, Fe, Al, Si, Ti and K) (see Fig. S1 and S2 in Supplement). Since absolute element concentrations are required for linear end-member mixing, we also

tested which element XRF scanner counts could be satisfactorily calibrated by linear regression with their corresponding powder XRF data. Such linear calibrations were found statistically acceptable for the elements Fe, Ca, Ti and K (see Fig. S3 in Supplement). All reference samples were also freeze dried, powdered and analyzed by EDP-XRF spectroscopy.

3.2.3. Rock magnetic analyses

Remanence-based magnetic analyses at room temperature were performed on all reference samples using the fully automated *2G SQUID* Rock Magnetometer at the University of Bremen Magnetics Lab with the same routines that were previously applied to the marine core samples (Leng et al., 2018). Anhysteretic remanent magnetization (ARM) is preferentially acquired by fine-grained magnetite (King et al., 1982; Frederichs et al., 1999). It was induced in a 40 μT direct field and an alternating magnetic field decaying from 100 mT. Isothermal remanent magnetization (IRM) was acquired over 23 field steps from 0 to 700 mT with an inline pulse coil of the magnetometer and five further magnetization steps up to maximum field of 2700 mT applied with an external pulse coil. This peak field IRM is referred to

as saturation IRM (SIRM). IRM acquired at 100 mT (IRM_{100mT}) primarily reflects the concentration of ferrimagnetic minerals and is less grain size selective than ARM (Frederichs et al., 1999). The ARM_{100mT}/IRM_{100mT} ratio is therefore a magnetogranulometric proxy with smaller values indicating larger grain size (Maher, 1988). The concentration of the high-coercive antiferromagnetic minerals hematite and goethite is represented by "hard IRM" (HIRM = $SIRM-IRM_{300mT}$; Stoner et al., 1996). Here we use the HIRM/IRM_{100mT} ratio as proxy for the proportion of hematite to magnetite content.

3.2.4. Estimating elemental composition of grain-size fractions

The volumetric mixing proportions of grain-size fractions control the composition of the mixture and can thus be utilized to obtain multi-property characteristics of volumetric sedimentary grain-size fractions (Just et al., 2012a). To obtain the elemental properties of the IRD and plumite sediment fractions, in a first step the volumetric proportion of the fractions finer and coarser than 30 μm was calculated for each sample. We used these volumetric mixing proportions of the fine and coarse fraction A and the elemental composition X to predict their unknown elemental properties S according to Eq. (1) (Just et al., 2012a).

$$X = A * S + E = \hat{X} + E$$

(1)

The data matrix $X(n,m)$ contains n observations (samples) of m properties (e.g., grain-size or element content), $S(k,m)$ represents k mixed sediment sources with their m properties, $A(n,k)$ delineates their n mixing proportions (for each sample). $\hat{X}$ represents the estimates of X that are explained by the model and $E(n,m)$ is a matrix of residuals. Since only S is unknown, this linear problem can be solved using non-negative least-squares fitting (NNLSQ, Löfberg, 2004) with introduced non-negativity and additivity constraints. A correlation coefficient analogous to Pearson's product-moment correlation coefficient was calculated for the measured and the estimated compositional data. The significance of this correlation was assessed using a Monte Carlo randomization test with 10^5 iterations.

4. Results

4.1. Properties of outburst flood deposits

4.1.1. Major element ratios of cores 14, 15, 16

From the logged major element counts (Al, Ca, Fe, K, Si and Ti) of all three studied cores, the calibrated downcore major element proportions are shown in Fig. S2 (Supplement), while their ratios Ca/Fe, Al/Si and K/Fe are shown as calibrated mass ratios in Fig. 3. Ca contains anti-phase changes with the elements Ti, Fe, K, Al and Si, which is usually the sign that calcite is mostly of biogenic origin, while the other elements are within detrital terrigenous minerals (Fig. S2; Govin et al., 2014), except for H1 where detrital carbonate predominates (Piper and Skene, 1998). As previously described for the physical property and rock magnetic logs (Leng et al., 2018), all three core records are composed of two major units, where the upper unit above Heinrich layer 1 (H1) represents the evolution from deglacial to Holocene hemipelagic conditions on the SW Grand Banks Slope under conditions of a largely ice-free Gulf. The unit between H1 and H2 shows the five reddish plumite beds separated by hemipelagic interlayers, where the event bed thicknesses decrease from the deep core 14 that is most proximal to the Laurentian Channel to the shallower and distal core 16 while the interlayer thicknesses increase in-

versely (Fig. 3). In core 14, the Ca/Fe ratios have the lowest values of 0.8–1.1 in the plumite beds, slightly increase to ~1.5 in the interlayers, reach maxima of 6–8 in Heinrich layer 1, vary between 1 and 2 during late deglaciation, and increase to 3–4 at the beginning of the Holocene. Al/Si and K/Fe show similar, but reversed patterns, with nearly constant high plateau values within the plumite beds and sharp decreases at their boundaries; they are significantly higher (0.32–0.34 and 0.62–0.65, respectively) in the plumite beds compared to the interlayers and all postglacial sections. Cores 15 and 16 show variations in element ratios similar to core 14.

While the narrow scaling of the downhole logs (Fig. 3) cannot resolve variations between different plumite beds, the compilation of cross-plots in Fig. 4 provides evidence of gradual compositional changes from Oc2 to Oa1. The hematite/magnetite ratio HIRM/IRM100$_{mT}$ (Leng et al., 2018) was chosen as abscissa parameter for all plots since it nicely spreads out the data of the five events layers and separates them well from the hemipelagic and Heinrich layers (but not from the LGM sediments of core 16). By following the elongated data groupings of Fig. 4a from left to right (i.e. from the older to the younger events), a negative trend is observed for Ca/Si, delineating a gradual reduction in Ca content from Oc2 to Oa1 by about 25%. The Al/Si and Fe/Si ratios in Fig. 4b and c, increase by ~6% and ~12% respectively through the same plumite sequence. Since absolute K and Ti counts remain nearly invariant (Fig. S2), their K/Fe ratios (Fig. 4d) and Ti/Fe ratios (not shown) are controlled by the increasing Fe content and therefore decrease slightly from Oc2 to Oa1. Except for the Fe/Si ratio, the element ratios of the plumite beds contrast significantly with those of the interlayers and hemipelagic deglacial and Holocene strata.

#### 4.1.2. Major element contents of IRD and plumite grain-size fractions

20 new grain-size distribution curves of Core 14 (Fig. 5a, blue lines) are shown together with curves of Core 16 (Fig. 5a, grey lines, Leng et al., 2018), both measured using identical laboratory procedures. In both cores, the grain-size distributions of the reddish event layers are composed of at least two discrete grain-size fractions, which are mixed at different proportions (Fig. 5b). The predominant fine fraction with modes of 6–10 μm and cut-off maxima at ~30 μm is thought to represent the outburst plume fallout (Leng et al., 2018). The second, much coarser and poorly sorted grain-size fraction is interpreted as IRD input. The grain-size distribution data (Fig. 5a) also shows that the proximal Core 14 contains less IRD content than the distal Core 16 (Leng et al., 2018), which is an interesting aspect for later discussion (Chapter 5.2). The presence of another omnipresent minor grain-size mode centered at ~20 μm is noted, but has no clear-cut explanation at present.

The estimated major element compositions of the <30 μm and >30 μm fractions should indicate whether the IRD and plumite fractions originate from the same source area. Because the coarse fraction of Core 14 is mostly below 2%, only Core 16 was used for the calculation. The results reported here (Fig. 5c) are significant at the 0.0005 α level. According to the estimated properties, the IRD (>30 μm) fraction of Core 16 contains about twice as much Ca, while the Al and K contents are about half those of the plumite fraction (<30 μm). Fe and Ti are moderately enriched and Si is slightly depleted in the plumite fraction compared to the IRD fraction.

4.2. Properties of source reference samples

Based on joint similarity in all available properties, as well as geological and geographical context, eight relatively coherent regional-lithological groupings were determined which contain 46 of the   refer-
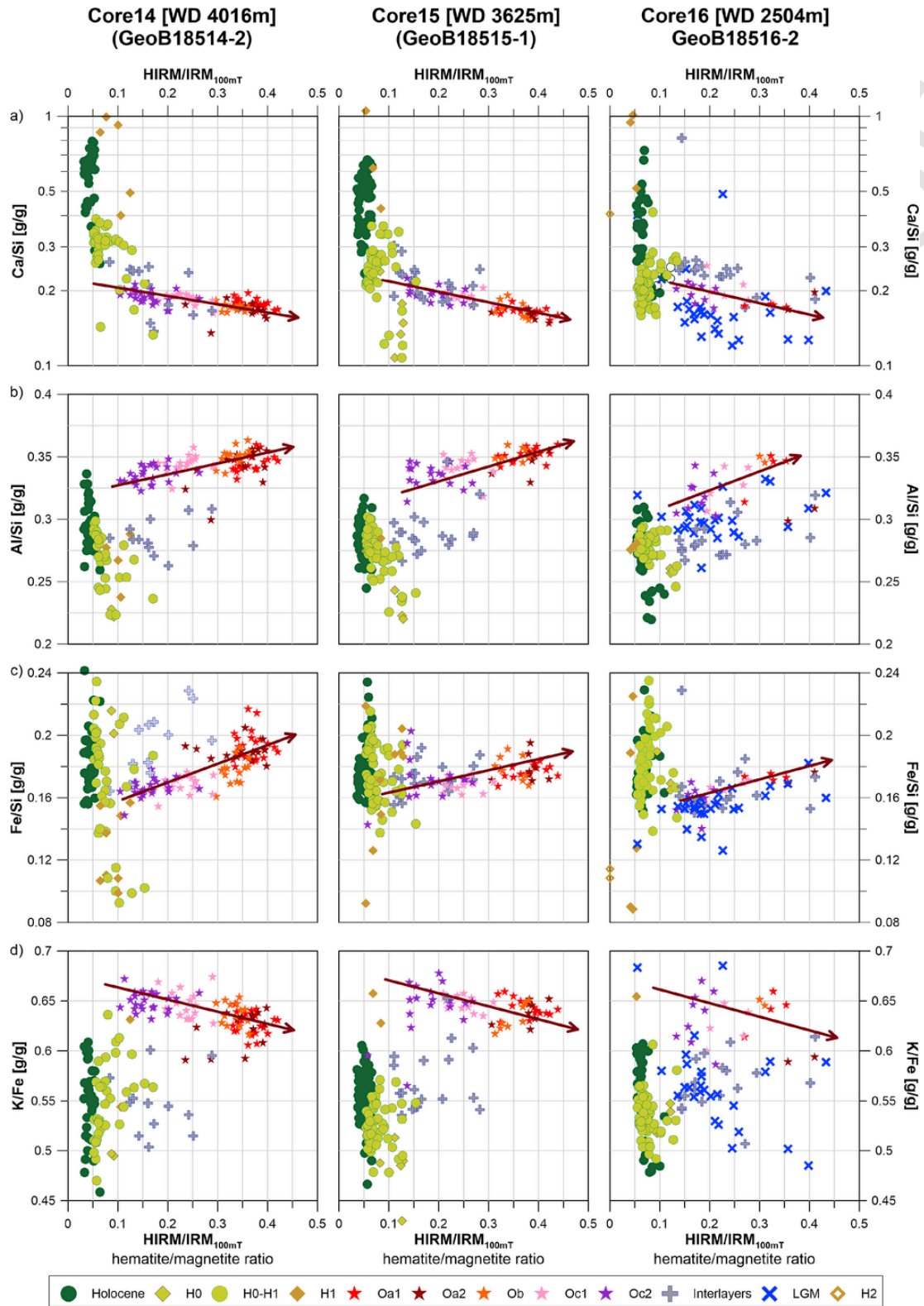
Fig. 4. Compiled cross plots of element ratios (Ca/Si, Al/Si, Fe/Si and K/Fe) against HIRM/IRM$_{100mT}$ (hematite/magnetite ratio) for cores 14, 15 and 16. HIRM/IRM$_{100mT}$ data are from Leng et al. (2018). Arrows (in red) show trends from Oc2 to Oa1. H0: Younger Dryas; H1: Heinrich layer 1; LGM: Last Glacial Maximum; H2: Heinrich layer 2. (For interpretation of the references to color in this figure legend, the reader is referred to the Web version of this article.)
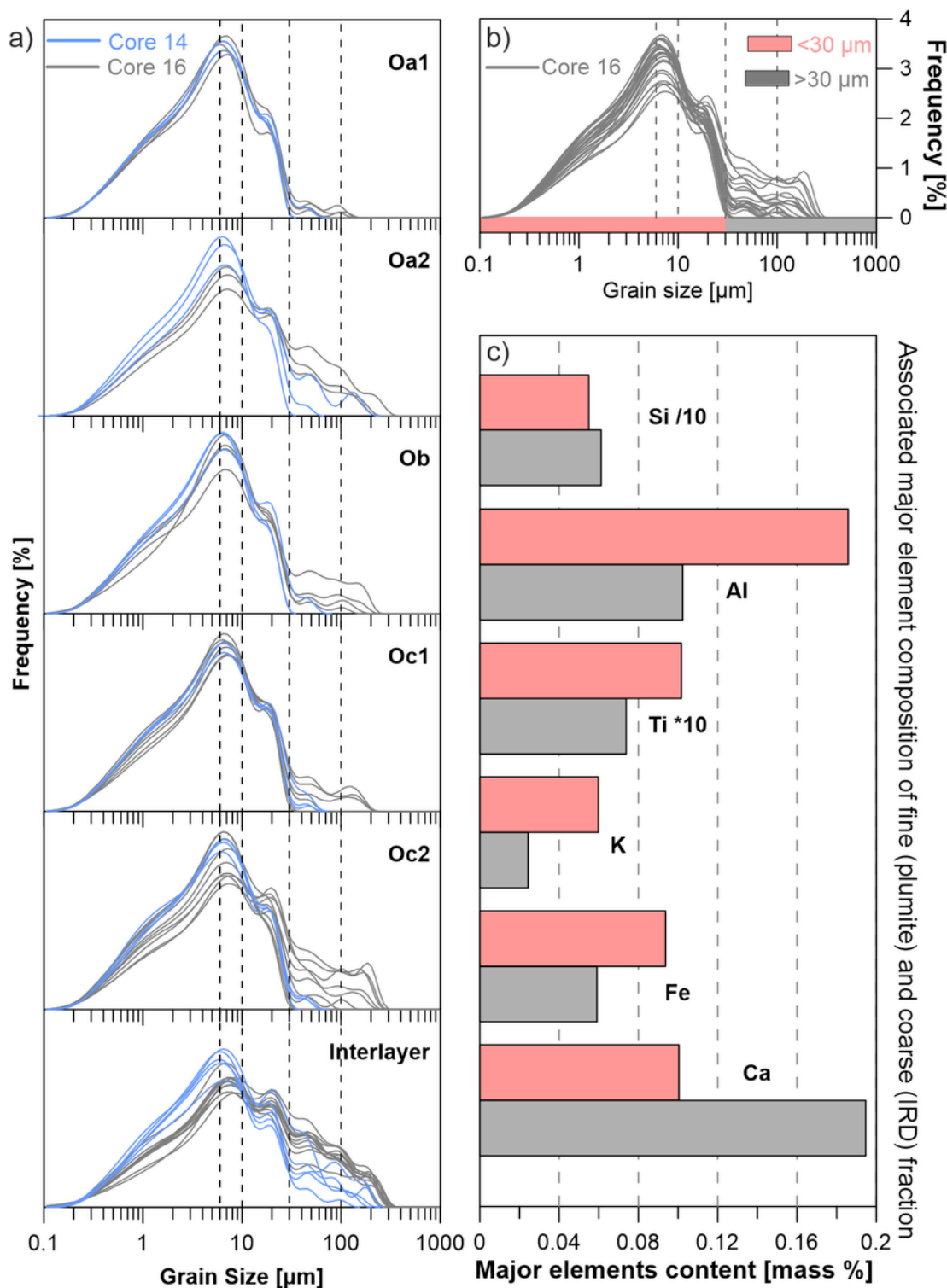
Fig. 5. (a) Grain-size distribution curves of plumite layers Oc2 to Oa1 and interlayers of core 14 (blue lines) and 16 (grey lines, Leng et al., 2018). **(b)** Grain-size distribution curves of all plumite layers of core 16 divided into finer, primarily plume-transported (red, <30 μm) and coarser, ice-rafted (grey>30 μm) grain-size fractions. **(c)** Associated major element concentrations of both fractions. (For interpretation of the references to color in this figure legend, the reader is referred to the Web version of this article.)

ence samples (Fig. 6). Table 1 lists chosen characteristic acronyms, the number of analyzed samples, source regions, host-rock lithology, as well as mean magnetic characteristics of these eight reference sample groupings. The remaining 34 coastal samples were discarded since they apparently represent intermediates, i.e. mixtures of geolog-

ically differing source areas (e.g. riverine sediments) or show signs of diagenetic (iron mineral sulfidization) or anthropogenic overprint (metallic contaminants in harbor areas) (Fig. S4). This grouping approach is substantiated by the bi-plots in Fig. 6 where each reference
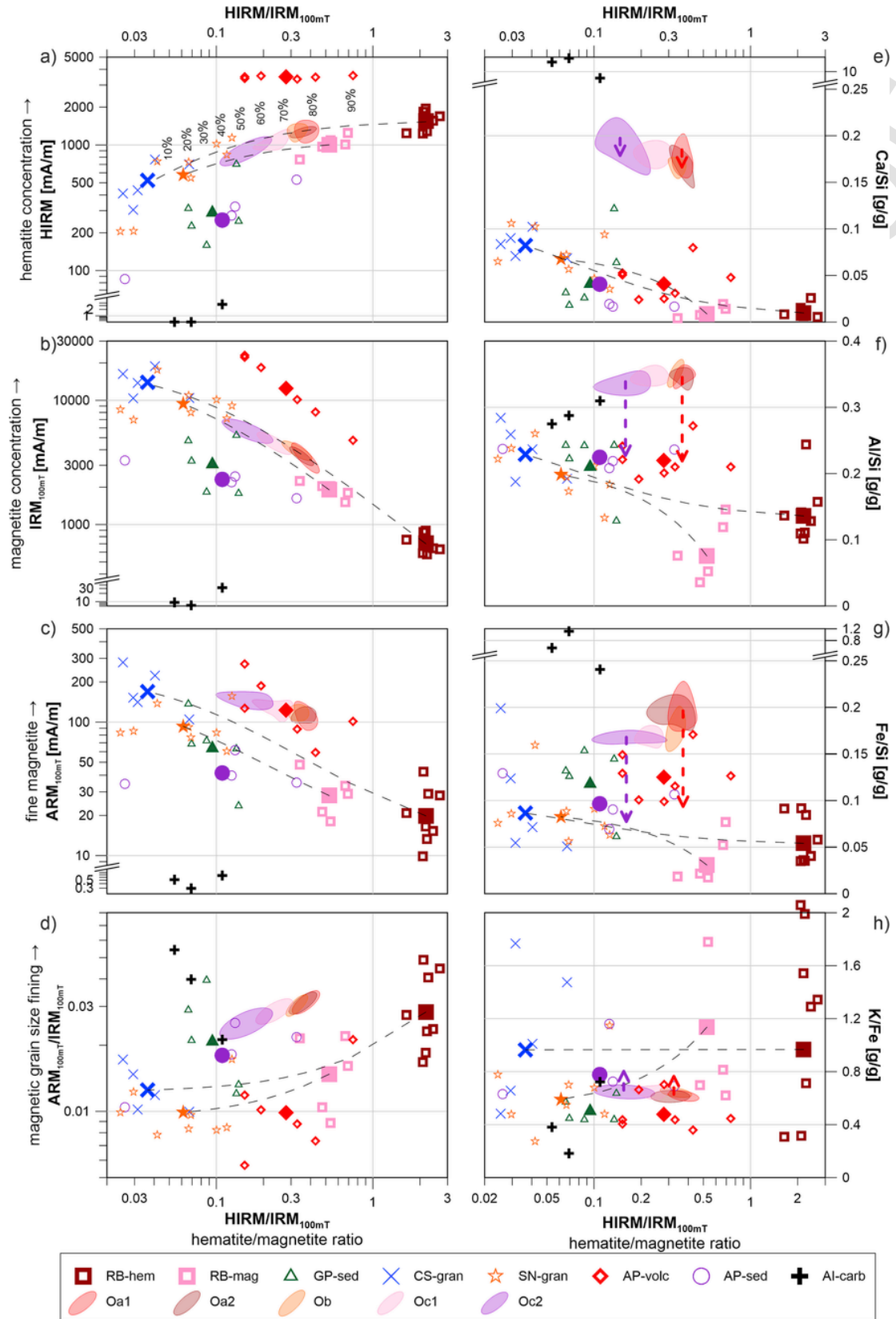
Fig. 6. Magnetic properties and major element ratio bi-plots of reference samples (symbols) and core data of plumite layers (envelope) against HIRM/IRM$_{100mT}$. **(a–d)** Magnetic parameters HIRM, IRM$_{100mT}$, ARM$_{100mT}$ and ARM$_{100mT}$/IRM$_{100mT}$. **(e–h)** Major element ratios Ca/Si, Al/Si, Fe/Si, and K/Fe. Reference samples are classified in 8 groups with colors as in Fig. 1. Larger filled symbols mark the geometric mean of each group. Elongated envelopes from purple to ruby red encircle the event bed data of Core 14 (Leng et al., 2018),

Oc2 - Oa1 with colors as in Fig. 4. Dotted lines delineate linear mixing curve of end-member group mean value. Dashed arrows indicate element ratio shifts of plumites by partitioning effect. (a-c, e and g) Note break in the ordinates to fit in the AI-carb sample points. (For interpretation of the references to color in this figure legend, the reader is referred to the Web version of this article.)

Table 1
Reference sample groups, host rock and magnetic properties.

Source sample groups	Sample locations	Host rock lithology	Mean IRM [mA/m]	Mean HIRM [mA/m]	Mean HIRM/IRM	Number of samples
RB-hem	Northern Nova Scotia, Prince Edward Island	Reddish Appalachian Permo-Carboniferous sandstones and siltstones	700	1529	2.18	8
RB-mag	Northern Nova Scotia, Prince Edward Island	Reddish Appalachian Permo-Carboniferous sandstones and siltstones	1907	1002	0.53	5
GP-sed	Gaspé Peninsula	Ordovician and Silurian sedimentary rocks	3055	287	0.09	5
CS-gran	Canadian Shield (upper St. Lawrence Estuary northern bank)	Precambrian crystalline igneous and metamorphic rocks	13,566	493	0.03	5
SN-gran	Southern Newfoundland	Cambrian to Devonian metamorphic and granitic rocks	9384	576	0.06	8
AP-volc	Newfoundland Burin and Avalon Peninsula	Reddish Neoproterozoic volcanic rocks	12,470	3479	0.28	8
AP-sed	Newfoundland Avalon Peninsula	Neoproterozoic sedimentary rocks	2311	251	0.11	4
AI-carb	Anticosti Island	Grey Ordovician-Silurian carbonate rocks	16	1.5	0.09	3

sample group has different and characteristic ranges of values for rock magnetic and compositional properties.

4.2.1. Magnetic properties of reference samples

In the first column of Fig. 6, delineating magnetic remanence properties (Fig. 6a–d), the hematite-magnetite proxy $HIRM/IRM_{100mT}$ was again chosen as abscissa value (as in Fig. 4). The volcanic rocks of Avalon Peninsula (AP-volc, red) have the highest absolute hematite content (Fig. 6a) with consistently high HIRM values of ~4000 mA/m. However, this group ranks in the mid-range of the $HIRM/IRM_{100mT}$ ratio scale, as their IRM_{100mT} values indicative of magnetite concentration are also very high (5000–20,000 mA/m, Fig. 6b). Second highest are the Appalachian red-bed sediments with typical HIRM hematite values of ~1000–2000 mA/m (Fig. 6a). Interestingly, these samples fall into two groups: RB-hem (brown) and RB-mag (pink). The first group RB-hem has higher hematite content and accordingly the highest observed $HIRM/IRM_{100mT}$ ratio of ~2–3, while the second group RB-mag features a slightly lower hematite (Fig. 6a) and a 3–4 times higher magnetite content (Fig. 6b), lowering its $HIRM/IRM_{100mT}$ ratio to ~0.5. The granitic samples from southern Newfoundland (SN-gran, orange) are in the mid-range with HIRM values of ~500-1000 mA/m, and due to their much higher magnetite content, their $HIRM/IRM_{100mT}$ ratio is only at ~0.1 (Fig. 6a and b). At the lowest end of the $HIRM/IRM_{100mT}$ scale are the granitic and metamorphic rocks of the Canadian Shield (CS-gran, blue) with values of ~0.03, resulting from their lower hematite HIRM values of 300–800 mA/m contrasting with their very high magnetite IRM_{100mT} values of 10,000–20,000 mA/m (Fig. 6a and b). While group AP-volc lies above all other groups, the four subsequent groups (RB-hem, RB-mag, SN-gran and CS-gran) form a curved band, which embraces all data points of the plumite beds in its center (Fig. 6a and b). At a distance below this band lie the two hematite- and magnetite-poor sedimentary rocks of Gaspé Peninsula (GP-sed, green), Avalon Peninsula (AP-sed, purple) and Anticosti Island (AI-carb) with $HIRM/IRM_{100mT}$ ratios of 0.03–0.3. Their very low hematite HIRM values of 100–500 mA/m (AI-carb 0.5–5 mA/m) and comparably low magnetite IRM_{100mT} values of 2000–5000 mA/m (AI-carb 7–30 mA/m) set these groups apart from all other reference sample groups and the plumite data (Fig. 6a and b).

In the two lower bi-plots (Fig. 6c and d), ARM_{100mT} represents mainly fine, submicron-sized magnetite as known e.g. from magnetic inclusions in silicate minerals (Hatfield et al., 2016) or as biogenic magnetite (Vali et al., 1989). The declining trend of ARM_{100mT} with $HIRM/IRM_{100mT}$ (Fig. 6c) over one order of magnitude (~200-20 mA/m) follows the total magnetite content (Fig. 6b) in most features. The similar covariance of fine and total magnetite content with the hematite/magnetite ratio suggests that both are from a common detrital source, since the alternative option, magnetite biomineralization in the sediment, should be independent from and not covariant with detrital magnetite input. Magnetogranulometric ARM_{100mT}/IRM_{100mT} ratios of ~0.01 (Fig. 6d) indicate that the magmatic source sample groups (CS-gran, SN-gran, and AP-volc) carry the coarsest magnetite crystals. With ratios of 0.01–0.02, the CS-gran and RB-mag groups have slightly coarser magnetite than the RB-hem, GP-sed, AP-sed, and AI-carb groups, whose ARM_{100mT}/IRM_{100mT} ratios of 0.02–0.05 are similar to those of the plumite beds (Fig. 6d).

4.2.2. Major element contents of reference samples

The second column of Fig. 6 compares major element ratios of reference and core samples (Fig. 6e–h). For all siliceous sources, Ca/Si ratios are low (Fig. 6e) and range from ~0.05 to ~0.1 in case of magmatic and from ~0.01 to ~0.05 for sedimentary host rocks. The calcareous Anticosti samples (AI-carb) have high Ca/Si ratios of 5–35, far away from the other groups. We note that the Ca/Si ratios (~0.15–0.2) of the plumite beds are clearly higher than those of the purely siliceous sources, but also still very far from the calcareous group (AI-carb).

The Al/Si and Fe/Si ratios (Fig. 6f and g) vary similarly and in absolute numbers much less than the Ca/Si ratio. These two grain-size sensitive ratios (section 2.2) show considerable scatter along the declining trend formed from Al- and Fe-rich magmatic groups (CS-gran, SN-gran, AP-volc) exhibiting high Al/Si and Fe/Si ratios (~0.15–0.25 and 0.05–0.2, respectively), to the red-bed groups (RB-hem, RB-mag) showing lower Al/Si and Fe/Si ratios (~0.05–0.15 and ~0.01–0.1). In both cross-plots, the grouping of the plumite layers exhibits rather well confined Al/Si and Fe/Si ratios of ~0.35 and ~0.2, respectively (Fig. 6f and g), and is vertically offset from the main trend formed by reference samples. Finally, in Fig. 6h, the K/Fe ratios (like the Ti/Fe ratio, not shown) of all source reference groups show rather similar, hence source-unspecific mean values with high internal variability. With values of ~0.6, the K/Fe ratio of the plumite layers falls right into the scattered data cloud of most reference samples (Fig. 6h).

5. Discussion

5.1. Compositional differences between plumite and hemipelagite units

The new elemental data (Figs. 3 and 4) supports and complements the previous rock magnetic evidence (Leng et al., 2018) that the composition of the five plumite beds at the SW Grand Banks Slope differs fundamentally from those of their hemipelagic interlayers and subsequent deglacial (H1 to H0) and Holocene sediment units. Compared to the hemipelagites, the plumites are characterized by lower Ca/Si ratios (strictly terrigenous/detrital plumites vs. partly marine sourced hemipelagites) and higher Al/Si and K/Fe ratios (more sedimentary vs. more magmatic sources). The redness of the plumites reflecting their very high hematite content (Fig. 6a) points to a Laurentian, specifically Appalachian provenance (Needham et al., 1969; Alam and Piper, 1977; Piper et al., 2007), suggesting a sedimentary source of hematite with red sandstones and shales (RB-hem and/or RB-mag). However, their relatively higher magnetite contents (Fig. 6b) imply that the event beds must also have received contributions from igneous sources, introducing granitic and metamorphic Canadian Shield rocks (CS-gran) and possibly granitic formations of the Newfoundland terrain complex (SN-gran) into the range of important provenance areas.

By comparing data variability of both sediment types in Fig. 4, it is noted that the individual plumite beds have well-defined geochemical properties that change systematically from the oldest to the youngest event, suggesting a systematic compositional evolution of the Laurentian Channel source during its glaciated phase. The hemipelagic units are compositionally less confined than the plumites and typically vary over the full ordinate range. Since their marine $CaCO_3$ contents are below ~20–30% (estimated from Ca content, Fig. S2), this large compositional variability is not primarily due to changing marine carbonate sedimentation but rather an expression of varying input from geologically contrasting detrital sediment sources.

5.2. Impact of partitioning effects on plumite composition

Provenance studies are notoriously confronted with the problem that compositional properties of the conveyed sediment source fractions no longer fully resemble those of their source materials (Nesbitt et al., 1996; Garzanti et al., 2009). The reasons are multifold and include hydraulic grain-size, mineral-shape and -density fractionation, varying resistance against physical abrasion and chemical dissolution or alteration of particles during transport. In our case, we have three successive partitioning steps, where the first proceeds from glacial bedrock erosion to glaciomarine deposition in the ice-stream channel-bed, the second results from the winnowing effect of turbulent subglacial sheet flow during meltwater outburst floods, and the third is due to selective gravitational settling from an expanding hyperpycnal plume. We may argue that the first partitioning step is already included by our sampling concept of collecting freshly eroded near-shore sediments, mainly eroded from glacial till, instead of host rock. Modern erosion involves chemical weathering, pedogenesis and atmospheric conditions that certainly produce a different mineral and grain-size mixture compared to that eroded by an overpassing glacier. However, we suggest that the cold climate conditions of the St. Lawrence Gulf region still favor physical over chemical weathering (Loring and Nota, 1973). For the second and third type of partitioning processes, we can only argue with predicted or derived grain-size sensitivities of various magnetic and elemental properties.

5.2.1. Major element partitioning by subglacial and proglacial transport processes

The associated compositional properties of coevally deposited plumite and IRD fractions (Fig. 5) shed some light on the selectivity of glacial erosion, the subglacial outwash process, and transport in hyperpycnal plumes. We argue that meltwater outburst events and glacial surges were causally connected and largely synchronous as suggested by the proportionally high accumulation rates of IRD and plume deposition over short event periods. During this bimodal sediment export, the generally coarser ice-rafted fraction is probably the better analogue of source rock composition.

The same argument also accounts for the poorly sorted ice-eroded material that was deposited in the Laurentian Channel bed by converging branches of the LCIS, until it was winnowed and partitioned by an outwash event. Comparing the element-specific fractionation ratios of Figs. 2b and 5c, we find that the meltwater outwash and subsequent hyperpycnal flow primarily mobilized finer particles with enhanced Al, Fe, K and Ti contents. Not surprisingly, these are typical elements of hard crystalline rocks whose fragments are ground to silt- and clay-size during the long subglacial transport from the interior Canadian Shield.

Contrastingly, the Ca content of the plumite beds is by a factor of two higher in the IRD fraction than in the plumite fraction (Fig. 5c). As biogenic carbonate content is very minor (Gil and Keigwin, 2018), the Ca must essentially originate from calcareous bedrock of the wider Anticosti Island region. The deep striations in the modern landscape of Anticosti Island (Eyles and Putkinen, 2014) are evidence of glacial erosion of limestone and dolomite. The relatively narrow west-east oriented band of Paleozoic limestones is only a short distance away from the LCIS channel bed, probably too short to efficiently disintegrate entrained calcareous detritus. The Ca content of Laurentian Channel sediments should therefore be under-represented in the outburst deposits. The element Si occurs in comparable concentrations in a wide range of silicate minerals and grain sizes, and is therefore much less affected by partitioning (Fig. 5c). The higher relative sand/silt ratio at the more distal core site 16 compared to site 14 (Fig. 5a) is in inverse relationship to the event bed thicknesses of both cores (Fig. 3). We hypothesize, that the channeling of the hyperpycnal plume by the Laurentian Fan canyons primarily focused the plumite deposition to its more proximal overspill areas, while the coarser ice-rafted sediment was more evenly dispersed over the wider Laurentian Channel outflow region, leading to higher IRD proportions at the margins of the outburst plume.

The above postulated element enrichment and depletion by transport partitioning should be mirrored in the relationships of our source reference and plumite data (Fig. 6). Indeed, we find that the range of characteristic Al/Si (0.33–0.35) and Fe/Si (0.17–0.22) ratios over the entire event bed sequence exceed all observed reference materials by approximate factors of ~1.7 and ~2.5, respectively (Fig. 6f and g). However, the element ratios of the plumites match very well the averaged Al/Si ratios (0.34) and Fe/Si ratios (0.25) of 18 clay samples taken from the modern Laurentian Channel and its side arms (Loring and Nota, 1973). The systematic disagreement of plumite composition with coastal reference samples and agreement with redeposited channel-bed samples underline, that the modern sediment transport from coast to channel-bed produces essentially the same Al/Si and Fe/Si partitioning factors as the subglacial outwash events did. From grain-size fractionated averaged elemental concentrations of Gulf of St. Lawrence sediments given by Loring and Nota (1973) (Fig. 2), we calculate that Al/Si and Fe/Si ratios from sand (500-53 μm) to fine silt (16-2 μm) fractions increase by factors of 1.5 and 1.75, and from sand to clay (<2 μm) by factors of 2.1 and 4.0, respectively (Fig. 2b). Our

observed partitioning factors (∼1.7 for Al/Si and ∼2.5 for Fe/Si as explained above) fall within these two estimates and seem therefore reasonable. When applying these estimated correction factors to the groupings of the event beds, these groupings fall directly onto the main mixing trend of the source reference data (Fig. 6f–h, vertical dashed arrows).

For the K/Fe ratio (Fig. 6h), the corresponding correction factors of 0.87 (fine silt vs. sand) and 0.55 (clay vs. sand) from Loring and Nota (1973) (Fig. 2) also comply with the observed offset between plumite and reference values corresponding to a reduction factor of ∼0.65–0.75. The Ca/Si ratios (Fig. 6e) of the plumite beds (0.17–0.22) are ∼5 times higher than the general trend of our siliceous reference samples (0.01–0.1) samples, but still much smaller than the calcareous Anticosti Island samples (5–35). Based on Loring and Nota (1973) data, the impact of grain-size partitioning on Ca/Si ratios is small if not negligible. To account for the comparably high Ca/Si ratios of the plumite deposits, a terrestrial carbonate contribution is therefore inferred.

5.2.2. Magnetic mineral partitioning by subglacial and proglacial transport processes

Although the impact of grain-size partitioning on major element and mineral content has been extensively studied (e.g. Loring and Nota, 1973; Garzanti et al., 2009), the gravitational partitioning of magnetic (i.e. heavy) minerals in suspension transport is less well documented. Isolated magnetite particles are known to enrich frequently in energetic littoral accommodation spaces such as tidal channels and nearshore zones (e.g. Badesab et al., 2012, 2017) where their exceptionally high density hinders bedload transport and fosters the formation of magnetic placer deposits.

The magnetogranulometric ARM_{100mT}/IRM_{100mT} ratio (Fig. 6d) shows a considerable partitioning effect between the coarser magnetite grain sizes of the source reference samples (0.01–0.03) and the relatively finer plumite beds (0.02–0.04), in particular with regard to magnetite-rich source materials. Biogenic magnetite played no relevant role for the magnetic mineral assemblage of our reference samples since it would have increase ARM_{100mT}/IRM_{100mT} ratio towards higher characteristic ratios of ∼0.1 (Franke et al., 2007). Plumites have systematically higher ARM_{100mT} values (Fig. 6c) of 100–200 mA/m than the main trend of the source rocks (20–80 mA/m). Only the magmatic groups (CS-gran and AP-volc) contain as much fine magnetite (ARM_{100mT} of 100–300 mA/m) as the plumite events, but their total magnetite concentration is too high (Fig. 6b, d) to be the dominant source rock for the plumite beds.

Magnetic minerals are very efficiently entrained along with lighter siliceous minerals if they reside as small Fe oxide inclusions in quartz or feldspar grains (Hounslow and Maher, 1996; Hounslow and Morton, 2004), as attachments in clay mineral aggregates (Franke et al., 2007), or as staining hematite coatings on the surfaces of quartz grains as in the case of red-bed sediments (Piper and Slatt, 1977; Bond and Lotti, 1995). Such fine embedded magnetic mineral crystals did not experience gravitational fractionation during suspension transport but followed the partitioning of their host grains. A rock magnetic comparison of corresponding plumite layers in cores 14, 15 and 16 shows only very modest decrease in hematite and magnetite content (Leng et al., 2018) from proximal to distal locations off the Laurentian Fan, while some magnetic grain-size fining (ARM_{100mT}/IRM_{100mT}) is observed.

Comparing the hematite and magnetite content of plumite with all reference sample data (Fig. 6a and b), we observe no off-trend shifting of the plumite groupings in contrast to the major element ratios. The central positions of the narrowly clustered and successively

shifted data points corresponding to outburst layers Oc2-Oa1 on the mixing band between red-bed sediments (RB-hem and RB-mag) and magmatic bedrock (CS-ign, SN-gran) implies that both these source end-members contributed to LCIS channel-bed sediments. Transport does not seem to have biased absolute or relative hematite and magnetite concentrations much.

5.3. Impact of source mixing on plumite composition

With this improved understanding of magnetic and major element properties of sources and sinks as well as transport partitioning effects to apply, we now set up a deterministic multiple-source mixing model to quantify the changing source material contributions over the outburst event sequence. To keep this model as robust and transparent as possible, it is kept limited to those few (linear) rock magnetic and sedimentological parameters, which efficiently discriminate the main source-rock groups and show no or little impact by transport partitioning.

5.3.1. Deterministic mixing models of Laurentian Channel outburst sediments

As a first iteration to this source-mixing model, curvilinear mixing lines of the two most prominent source end-members have been added in all crossplots of Fig. 6. Along their mixing lines based on HIRM (hematite/goethite content, Fig. 6a) and IRM_{100mT} (magnetite/maghemite content; Fig. 6b), the plumite groupings Oc2-Oa1 comply with mixing proportions of 40–80% of the hematite-rich red-bed (RB-hem) source mean value and, accordingly, 60-20% of the magnetite-rich granite (CS-gran) source mean value. But only the carbonate-rich AI-carb source can explain the far higher Ca/Si ratios of the plumites relative to all other sources, which have consistently lower carbonate contents (Fig. 6e). In the linear parameters space of HIRM, IRM_{100mT} and Ca wt%, the three source mean values of RB-hem, CS-gran and AI-carb define a (red) planar mixing triangle (Fig. 7a and b) enclosing all plumite data with little lateral offset. We therefore use these three sources to define a deterministic ternary linear mixing system with respective hematite-, magnetite- and calcite-rich end-members *EM-H, EM-M* and *EM-C,* yielding notional mixing proportions C_{EM-i} for each given (plumite) sediment sample S by solving the linear equation:

$$\begin{pmatrix} IRM \\ HIRM \\ Ca\% \end{pmatrix}_S = C^*_{EM-H} \begin{pmatrix} IRM \\ HIRM \\ Ca\% \end{pmatrix}_{EM-H}$$
$$+ C^*_{EM-M} \begin{pmatrix} IRM \\ HIRM \\ Ca\% \end{pmatrix}_{EM-M}$$
$$+ C^*_{EM-C} \begin{pmatrix} IRM \\ HIRM \\ Ca\% \end{pmatrix}_{EM-C}$$

$$\text{with } C_{EM-i} = \frac{C^*_{EM-i}}{C^*_{EM-H} + C^*_{EM-M} + C^*_{EM-C}} \quad (2)$$

Here, the mixing coefficients must still be normalized to 100% to meet the additivity constraint, since data points that are laterally offset from the mixing triangle have proportions summing up to slightly less or more than 100%. To also include this offset in the unmixing result, a fourth "neutral" end-member compensating the residuals of

the mixing system is introduced. This additional end-member EM-D stands for diluting admixed sources that are low in magnetic mineral and Ca content (such as SN-gran, GP-sed) as well as for potential porosity and partitioning bias, extending the ternary mixing plane into a tetrahedral mixing space:

$$
\begin{pmatrix} IRM \\ HIRM \\ Ca\% \\ 1 \end{pmatrix}_S = C^*_{EM-H} \begin{pmatrix} IRM \\ HIRM \\ Ca\% \\ 1 \end{pmatrix}_{EM-H}
$$
$$
+ C^*_{EM-M} \begin{pmatrix} IRM \\ HIRM \\ Ca\% \\ 1 \end{pmatrix}_{EM-M}
$$
$$
+ C^*_{EM-C} \begin{pmatrix} IRM \\ HIRM \\ Ca\% \\ 1 \end{pmatrix}_{EM-C} + C^*_{EM-D} \begin{pmatrix} 0 \\ 0 \\ 0 \\ 1 \end{pmatrix} \qquad (3)
$$

The coefficient 1 in the last line of each data vector ascertains fulfillment of the additivity constraint when jointly solving the four linear equations for the four unknown coefficients. As long as analyzed data stays in the body angle from the origin over the sides of the mixing triangle, the mixing coefficients of *EM-H, EM-M* and *EM-C* are all positive (Fig. 7c and d), those of *EM-D* can have both positive (dilution by quartz or water) or negative (quartz depletion, dewatering) values (Fig. 7d).

5.3.2. Major source areas and their contributions to plumite beds Oc2 to Oa1

The bivariate diagrams (Fig. 6a and b) leave some uncertainty regarding alternative contributions of RB-hem or RB-mag and of CS-gran or SN-gran, since any pair of encountered red-bed and granite varieties spans mixing bands in the vicinity of the plumite samples. The 3D side perspective onto the mixing triangle (Fig. 7b) illustrates, better than the 2D plots, that plumite data are considerably displaced relative to other alternative mixing triangles with RB-mag vs. SN-gran or RB-mag vs. CS-gran baselines. The high hematite content of RB-hem is obviously required to provide sufficient hematite for the plumites, in particular for the youngest plumite beds Oa2 and Oa1 (Figs. 4 and 6a). Sampling sites of the most hematite-rich, but less magnetite-rich RB-hem group (Fig. 1) are, to our knowledge, only geographically, but not geologically separable from sites falling into the RB-mag group. It would require host rock sampling in these areas to find out if the contrasting magnetite/hematite ratios were inherited from the red-bed host rocks or formed later, e.g. by pedogenesis. Available thermomagnetic curves (data not shown) indicate that the magnetite of RB-mag is actually a maghemite, an oxidized form of magnetite and typical pedogenic mineral.

The low ARM_{100mT}/IRM_{100mT} ratios of RB-mag (Fig. 6d) exclude bacterial magnetite biomineralization and its presence on Prince Edward Island also speaks against fluvial admixture of magmatic hinterland rock. As the Appalachian red-bed area is much larger than our sampled sector (Fig. 1), any answer to this issue would still not necessarily cover all variability of the vast potential source area making up over 80% of the modern Gulf area. According to Fig. 7c and d, the Appalachian red-beds contributed increasingly to the plumite sediments, from 35 to 60% to layer Oc2, over 50–65% to layer Oc1, to 65–75% to layers Ob, Oa2 and Oa1.

A similar ambiguity exists regarding the roles of Canadian Shield (CS) and southern Newfoundland (SN) granites. According to our regionally-limited sample distribution, the CS-gran group has on average higher magnetite and lower hematite contents than the SN-gran group. Both sources qualify statistically and geologically as magnetite end-members, and we therefore compare the consequence of both options in Fig. 7c. When mixing CS-gran and RB-hem, we find that the contribution of granite end-member decreased from 50 to 30% during Oc2 to 40-25% during Oc1 and was at lower 25-15% during Ob, Oa2 and Oa1. Choosing SN-gran instead of CS-gran as magnetite-rich end-member, the granitic contributions reach higher proportions of 70–40%, 60-35%, and 35-25%, respectively, at the expense of the share of the red-beds. However, these relative shifts between both major granite sources do not affect the main results of this provenance study, while the much larger ice-erodible areas of the Canadian Shield offer potentially greater geological variability that outweighs the statistical uncertainty of our source samples.

Contributions from the calcareous source areas of the northern Gulf of St. Lawrence are smaller, more stable and better constrained by data. They decreased from 13 to 9% in Oc2 and Oc1 to 9-7% in Ob, Oa2 and Oa1 (Fig. 7c and d). Together, the mixing results provide for the first time volumetric estimates of changing source area contributions and thereby quantify the geochemical trends observed in Figs. 4 and 6.

Although the fourth (residual) end-member is excluded in the ternary mixing diagrams, the variability of EM-D nevertheless carries environmental information. EM-D has positive values of 5–15% for the oldest outburst event layer Oc2 (Fig. 7d), which may result from to the greater variability of end-members EM-M and EM-H and the comparatively large IRD component of this unit (Fig. 5); larger particles should contain more quartz and less fine-grained magnetite and hematite. Oc1 has lower IRD and EM-M contributions, reducing "dilution" effects to around 0–5%. For the three younger plumite beds Ob, Oa2and Oa1, the end-member EM-D takes generally negative values of −10 to −20% (Fig. 7d), indicating an enrichment in magnetic mineral content above the level of the ternary source reference system. As we discuss in the following, this may be due to a shift of the depocenter. This enrichment level is lower at bottom and top of these event beds and reaches 20% in the centers.

5.4. Conditions and impact of outburst floods from LCIS initiation to termination

The previous discussion sections demonstrated how source mixing and grain-size partitioning jointly control the rock magnetic and major element compositions of the five outburst flood deposits. Setting these results into a paleoclimatic, glaciological and geomorphological context (Fig. 8) reveals that the observed variations through time provide new details on the deglaciation history in the Gulf of St. Lawrence area.

5.4.1. Potential source depocenters for laurentian outburst flood deposits

Leng et al. (2018) argued that the compositional homogeneity and very large volumes of the outburst flood deposits required voluminous accommodation spaces in the Laurentian Channel to accumulate and premix sediments. Two prominent channel bed depressions (Fig. 8d, pink colors), both about 100 m deeper than the typical channel depth of ~400–430 m (Fig. 8d, green), may have been instrumental as depocenters. The upper of the two channel-bed depressions lies within the Gulf area; its greatest depth (560 m) is situated at Cabot Strait, the major geomorphological "bottleneck" of the LCIS, which corresponds to an ice divide in western Newfoundland (Fig. 8a). This
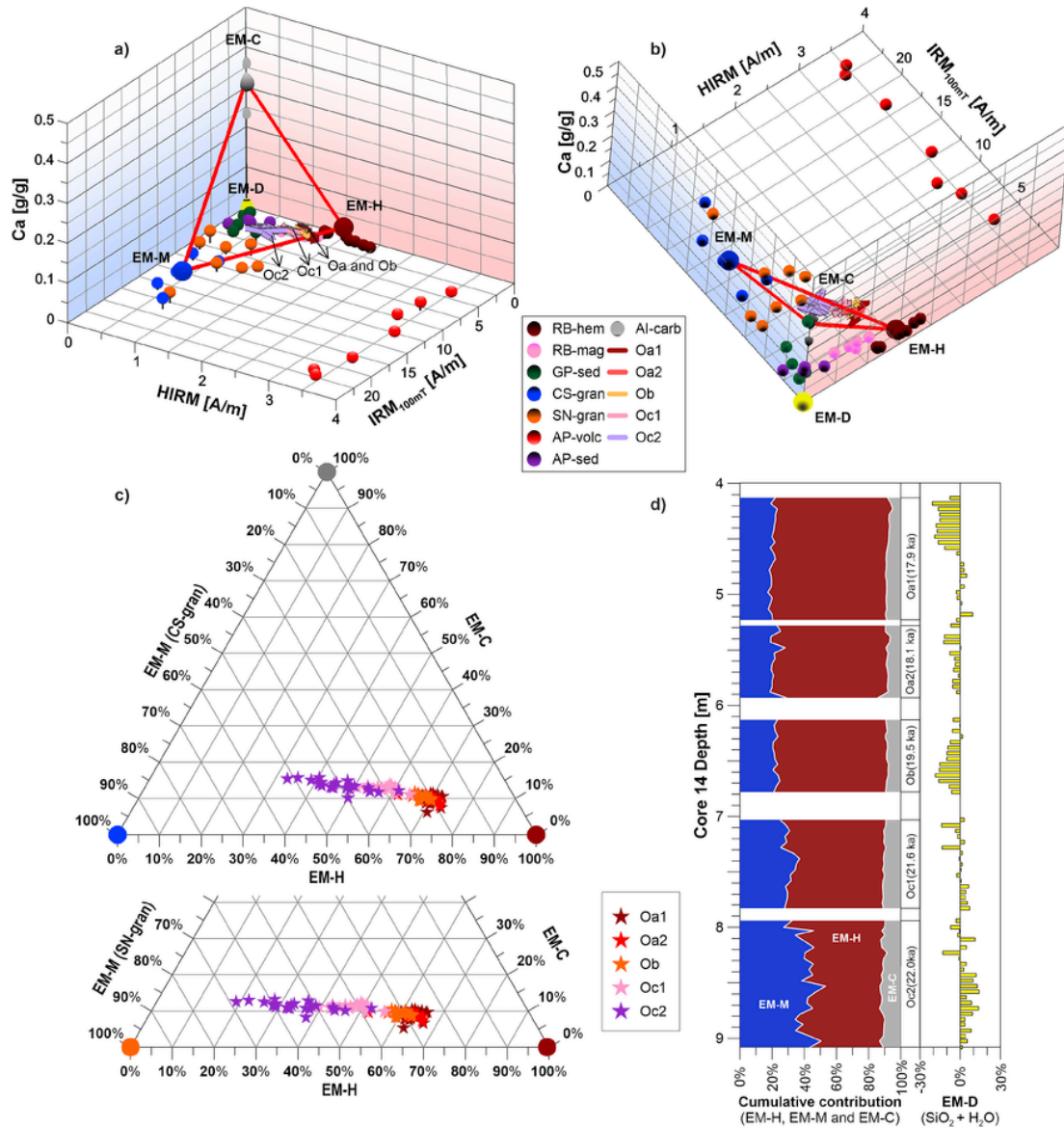
Fig. 7. **(a, b)** 3D plots of IRM_{100mT}, HIRM and Ca% values of Core 14 plumite beds Oc2 to Oa1 (colored lines), plotted into linear mixing models of averaged reference sample groups (colored symbols). Dots at the edges mark the chosen end-members for the calcareous EM-C in grey, the granitic source EM-M in blue, the red-bed source EM-H in ruby red and a non-magnetic, carbonate-free "diluting" source EM-D in yellow. **(c)** Positions of Core 14 event beds data in ternary mixing model of EM-C, EM-M and EM-H, where CS-gran (upper triangle) and SN-gran (lower triangle) are used as alternative granitic EMs. **(d)** Downcore cumulative proportions of EM-C, EM-M and EM-H and participation of EM-D.

"Cabot Depression" probably originates from increased glacial erosion caused by the lateral constriction of the LCIS. The eroded bedrock and till should have largely contributed to the downstream barrier of this depression, the Laurentian Moraine (LM), which is located just above the confluence of the LCIS with the southward-flowing Hermitage Channel Ice Stream (Fig. 8d) from SW Newfoundland. A second channel-bed depression of near equal size, depth and sill height exists between the LM and the shelf-edge Outer Laurentian Moraine (OLM). We informally refer to this mid-shelf basin next to Hermitage Channel as "Outer Laurentian Depression". The eastward rising slope of the Mesozoic basement (Todd, 2016) preformed this lower LCIS basin.

5.4.2. Conditions and sediment sources of initial outburst floods Oc2 and Oc1

The oldest two outburst events Oc2 (22.0 cal ka) and Oc1 (21.6 cal ka) both fall within the period when the Laurentian Ice Stream likely extended to the OLM as suggested by Shaw et al. (2006) (Fig. 8a), although dated material from this time at the ice margin is lacking. In this phase, the Outer Laurentian Depression primarily received glaciomarine or glaciolacustrine sediments from the LCIS and the tributary Hermitage Channel Ice Stream. The more granitic composition of plumite beds Oc2 and Oc1 (Fig. 7c and d) agrees well with input from both source areas, the Canadian Shield (Laurentide Ice Sheet) and SW Newfoundland (Newfoundland Ice Sheet) as indicated by the ice divides and flow lines in Fig. 8a. The relatively high carbonate content of these plumite events (Fig. 7d) should relate to the

intense glacial erosion of the Anticosti shelf, which Eyles and Putkinen (2014) explained by basal ice streaming from the hard, granitic Eastern Canadian Shield across the soft-bedded, calcareous Anticosti escarpment. The Oc2 sediments support this explanation by their extraordinarily high Ca partitioning ratio between IRD and the silt-clay phase (section 5.2.1). In this early phase, the Appalachian Ice Complex covering the Magdalen Shelf was still more static (Rémillard et al., 2017) and the influx of red-bed material was probably limited to existing deeper ice channels like the Chaleur Channel south of Gaspé Peninsula, the Western Cape Breton trough and the Esquiman Channel west of Newfoundland (Fig. 8a).

Following Margold et al. (2018), the LCIS activity started around 22.5–22.0 ka, coevally with the earliest post-LGM sea-level rise and in general coincidence with the less well dated oldest outburst flood event Oc2. The higher IRD content of plumite bed Oc2 relative to the subsequent plumite bed Oc1 suggests that the LCIS was still sediment-grounded upstream, since its sediment-bearing basal ice had not yet fully melted off. This first outburst event may have been instrumental in initiating the following more active phase of the LCIS. The second outburst event Oc1 happened under similar ice-stream and ice-margin conditions ~400 years later (Leng et al., 2018). Its noticeably higher content in Appalachian-sourced sediments (Fig. 7c and d) and much lower IRD content (Fig. 4a) indicate a growing input from the southern Gulf area, possibly driven by the flattening of the LCIS relief (induced by its higher flow rate) that increased the gradients of lateral ice-sheet surfaces.

5.4.3. Conditions and sediment sources of initial outburst floods Ob, Oa2 and Oa1

At around 19 ka, and possibly facilitated by event Oc1, the ice margin retreated from the shelf-edge to a position between Ban-quereau and St. Pierre Bank (Piper and Macdonald, 2001; Dyke, 2004, Fig. 8b), disabling further repetitions of the previous event scenario (Leng et al., 2018). This again lowered the gradient of the ice stream and improved conditions for another subglacial lake to develop and grow upstream in Cabot Depression. This lake would have accumulated sediment not only from the north, but increasingly from the west (and east?), as demonstrated by the higher hematite content from the soft-bedded Appalachian sandstones in Ob (Fig. 7c and d). Since the lower LCIS had turned into an ice shelf or had retreated to the LM, the LM and Cabot Strait bottleneck must have taken the role of a backstop against ice purging of the interior Gulf area. The first rapid post-LGM sea-level rise by ~10 m during meltwater pulse MWP-1A0 (19.6–18.8 ka; Clark et al., 2004; Lucchi et al., 2015) may have been influential in releasing the third outburst flood event Ob (19.5 ka) by uplifting grounded ice. As the sedimentary compositions of event bed Ob and the younger event beds Oa2 (18.1 ka) and Oa1 (17.9 ka) are practically identical, we presume that these three subsequent outburst events remobilized essentially the same glacial sediments from a subglacial lake depocenter localized in Cabot Depression. Whether these recurrent outflow events were triggered by sudden releases of upstream meltwater reservoirs, or by repeated breaching and reestablishment of the LM invoking rapid topographic gradient changes of the LCIS accompanied by turbulent sub-ice compensation flows, remains an interesting question that our data cannot answer. According to Josenhans and Lehman (1999), the ice-cover reached beyond Cabot Strait until about 16.5 ka and therefore permitted such recurrent scenarios (Fig. 8c). From ~16.5 ka, the LCIS and its major side channels were free of permanent grounded ice (Fig. 8d) and outburst flood scenarios such as those depicted above were no longer possible.
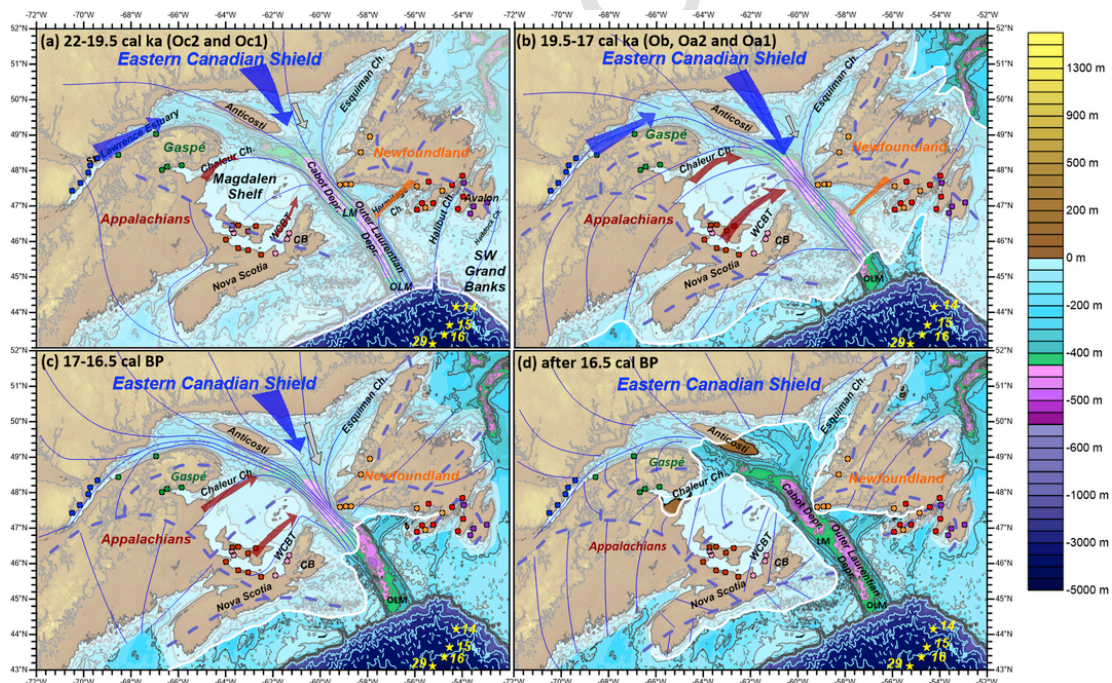
Fig. 8. (a–d) Retreat of ice margins (white layers) in the Gulf of St. Lawrence area from 22 to 16.5 ka. Ice margin positions were taken from (a) Shaw et al. (2006), (b) Dyke (2004), (c) and (d) Josenhans and Lehman (1999), revised by Piper and Macdonald (2001). Pink areas mark bathymetric depressions of 430–550 m water depths in the Laurentian Channel (green for 400–430 m). Blue dashed lines mark ice divides, thin blue lines indicate ice flow directions. Colored arrows represent sediment input from major source areas (red for EM-H, blue (CS-gran) and orange (SN-gran) for EM-M, grey for EM-C). Colored dots show coastal and estuary reference sample locations in the Gulf of St. Lawrence and off Newfoundland. Yellow stars denote core locations of Cores 14, 15, 16 and 29 (Leng et al., 2018). CB = Cape Breton, LM = Laurentian Moraine, OLM = Outer Laurentian Moraine, WCBT = Western Cape Breton trough. (For interpretation of the references to color in this figure legend, the reader is referred to the Web version of this article.)

6. Conclusions

New high-resolution major element and grain-size data of three previously studied sediment cores from SW Grand Banks Slope were measured to identify the sources of five event beds that were rapidly deposited during deglacial Laurentian meltwater outburst floods. Element ratios and rock-magnetic properties of these event beds were compared to a newly established reference sample set collected from potential source lithologies around the Gulf of St. Lawrence. Bivariate, ternary and tetrahedral mixing models of source end-members were set up to evaluate the source-to-sink processes and investigate changing source mixing between events, grain-size partitioning effects and the influence of deglacial ice retreat.

All three cores show similar element patterns, where the outburst event beds have fundamentally different composition compared to the hemipelagic interlayers and post-H1 units. The elemental Ca/Si and K/Fe ratios decrease (while the Al/Si and Fe/Si ratios increase) from the oldest outburst Oc2 to the youngest Oa1 event, suggesting compositional changes over the event sequence. The reference samples from the eight identified source areas have similar element ratios. Offsets between the element ratios of event beds and source sediments were quantitatively explained by grain-size and mineral partitioning during bedrock erosion, subglacial winnowing and suspension transport. The observed element enrichment or depletion rates match the grain-size dependent element partitioning of modern detrital Laurentian Channel sediments.

The magnetic properties of the reference samples group well and in accordance with bedrock types. Two Appalachian red bed sample groups represent a source of highly concentrated hematite, while two plutonic groups from the Canadian Shield and southern Newfoundland correspond to magnetite-rich granitic sources. All event bed data fell onto the mixing trend between hematite-rich and magnetite-rich sources. A deterministic ternary source-mixing model in the phase-space of IRM, HIRM and Ca% clarified that all plumite events were mixed from at least three main sources, where the earlier events (Oc2 and Oc1) had higher granitic and carbonate contributions and the later three events (Ob, Oa2 and Oa1) had consistently higher inputs from red bed sources. In the light of the Laurentide Ice Sheet retreat history, it seems that the earlier two outburst plumes were sourced from a subglacial depocenter in the lower Laurentian channel (Outer Laurentian Depression) when the ice margin was grounded at the OLM until around 21 ka. The subglacial sediment of the later three outburst plumes must have accumulated in a depocenter upstream of Cabot Strait (referred to as "Cabot Depression") while the ice margin was grounded at the Laurentian Moraine.

Acknowledgments

Appendix A. Supplementary data

Supplementary data to this article can be found online at https://doi.org/10.1016/j.quascirev.2019.04.031.

References

Alam, M., Piper, D.J.W., 1977. Pre-Wisconsin stratigraphy and paleoclimates off Atlantic Canada, and its bearing on glaciation in Québec. Géogr. Phys. Quaternaire 31 (1–2), 15–22. https://doi.org/10.7202/1000048ar.

Alley, R.B., Blankenship, D.D., Bentley, C.R., Rooney, S.T., 1986. Deformation of till beneath ice stream B, West Antarctica. Nature 322, 57–59. https://doi.org/10.1038/322057a0.

Bond, G.C., Lotti, R., 1995. Iceberg discharges into the North Atlantic on millennial time scales during the last glaciation. Science 267 (5200), 1005–1010. https://doi.org/10.1126/science.267.5200.1005.

Badesab, F., von Dobeneck, T., Bryan, K.R., Müller, H., Briggs, R.M., Frederichs, T., Kwoll, E., 2012. Formation of magnetite-enriched zones in and offshore of a mesotidal estuarine lagoon: an environmental magnetic study of Tauranga Harbour and Bay of Plenty, New Zealand. Geochem. Geophys. Geosyst. 13, Q06012. https://doi.org/10.1029/2012GC004125.

Badesab, F., von Dobeneck, T., Briggs, R.M., Bryan, K.R., Just, J., Müller, H., 2017. Sediment dynamics of an artificially deepened mesotidal coastal lagoon: an environmental magnetic investigation of Tauranga Harbour, New Zealand. Estuar. Coast Shelf Sci. 194, 240–251. https://doi.org/10.1016/j.ecss.2017.06.017.

Batterson, M., Taylor, D., Bell, T., Brushett, D., Shaw, J., 2006. Regional ice-flow mapping, surficial geology and till geochemistry of the northern Burin Peninsula and adjacent Placentia Bay. Curr. Res. 06–1.

Casse, M., Montero-Serrano, J.-C., St-Onge, G., 2017. Influence of the Laurentide Ice Sheet and relative sea-level changes on sediment dynamics in the Estuary and Gulf of St. Lawrence since the last deglaciation. Boreas 46, 541–561. https://doi.org/10.1111/bor.12230.

Clark, P.U., McCabe, A.M., Mix, A.C., Weaver, A.J., 2004. Rapid rise of sea level 19,000 years ago and its global implications. Science 304 (5674), 1141–1144. https://doi.org/10.1126/science.1094449.

Dyke, A.S., 2004. An outline of North American deglaciation with emphasis on central and northern Canada. Dev. Quat. Sci. 2, 373–424. https://doi.org/10.1016/S1571-0866(04)80209-4.

Eyles, N., Putkinen, N., 2014. Glacially-megalineated limestone terrain of Anticosti island, Gulf of St. Lawrence, Canada; onset zone of the Laurentian channel ice stream. Quat. Sci. Rev. 88, 125–134. https://doi.org/10.1016/j.quascirev.2014.01.015.

Franke, C., von Dobeneck, T., Drury, M.R., Meeldijk, J.D., Dekkers, M.J., 2007. Magnetic petrology of equatorial Atlantic sediments: electron microscopy results and their implications for environmental magnetic interpretation. Paleoceanography 22, PA4207https://doi.org/10.1029/2007PA001442.

Frederichs, T., Bleil, U., Däumler, K., von Dobeneck, T., Schmidt, A.M., 1999. The magnetic view on the marine paleoenvironment: parameters, techniques and potentials of rock magnetic studies as a key to paleoclimatic and paleoceanographic changes. In: Fischer, G., Wefer, G. (Eds.), Use of Proxies in Paleoceanography. Springer Berlin Heidelberg, pp. 575–599. https://doi.org/10.1007/978-3-642-58646-0_24.

Garzanti, E., Andò, S., Vezzoli, G., 2009. Grain-size dependence of sediment composition and environmental bias in provenance studies. Earth Planet. Sci. Lett. 277 (3–4), 422–432. https://doi.org/10.1016/j.epsl.2008.11.007.

Gil, I.M., Keigwin, L.D., Abrantes, F., 2015. The deglaciation over Laurentian Fan: history of diatoms, IRD, ice and fresh water. Quat. Sci. Rev. 129, 57–67. https://doi.org/10.1016/j.quascirev.2015.10.006.

Gil, I.M., Keigwin, L.D., 2018. Last glacial maximum surface water properties and circulation over laurentian fan, western North Atlantic. Earth Planet. Sci. Lett. 500, 47–55. https://doi.org/10.1016/j.epsl.2018.07.038.

Govin, A., Chiessi, C.M., Zabel, M., Sawakuchi, A.O., Heslop, D., Hörner, T., Zhang, Y., Mulitza, S., 2014. Terrigenous input off northern South America driven by changes in Amazonian climate and the North Brazil Current retroflection during the last 250 ka. Clim. Past 10, 843–862. https://doi.org/10.5194/cp-10-843-2014.

Hatfield, R.G., Stoner, J.S., Carlson, A.E., Reyes, A.V., Housen, B.A., 2013. Source as a controlling factor on the quality and interpretation of sediment magnetic records from the northern North Atlantic. Earth Planet. Sci. Lett. 368, 69–77. https://doi.org/10.1016/j.epsl.2013.03.001.

Hatfield, R.G., Reyes, A.V., Stoner, J.S., Carlson, A.E., Beard, B.L., Winsor, K., Welke, B., 2016. Interglacial responses of the southern Greenland ice sheet over the last 430,000 years determined using particle-size specific magnetic and iso-

topic tracers. Earth Planet. Sci. Lett. 454, 225–236. https://doi.org/10.1016/j.epsl.2016.09.014.

Hatfield, R.G., Stoner, J.S., Reilly, B.T., Tepley III, F.J., Wheeler, B.H., Housen, B.A., 2017. Grain size dependent magnetic discrimination of Iceland and South Greenland terrestrial sediments in the northern North Atlantic sediment record. Earth Planet. Sci. Lett. 474, 474–489. https://doi.org/10.1016/j.epsl.2017.06.042.

Hemming, S.R., 2004. Heinrich events: massive late Pleistocene detritus layers of the North Atlantic and their global climate imprint. Rev. Geophys. 42, RG1005https://doi.org/10.1029/2003RG000128.

Heslop, D., 2015. Numerical strategies for magnetic mineral unmixing. Earth Sci. Rev. 150, 256–284. https://doi.org/10.1016/j.earscirev.2015.07.007.

Hounslow, M.W., Morton, A.C., 2004. Evaluation of sediment provenance using magnetic mineral inclusions in clastic silicates : comparison with heavy mineral analysis. Sediment. Geol. 171, 13–36. https://doi.org/10.1016/j.sedgeo.2004.05.008.

Hounslow, M.W., Maher, B.A., 1996. Quantitative extraction and analysis of carriers of magnetisation in sediments. Geophys. J. Int. 124 (1), 57–74, 18.

Josenhans, H., Lehman, S., 1999. Late glacial stratigraphy and history of the Gulf of St. Lawrence, Canada. Can. J. Earth Sci. 36, 1327–1345. https://doi.org/10.1139/e99-030.

Just, J., Heslop, D., von Dobeneck, T., Bickert, T., Dekkers, M.J., Frederichs, T., Meyer, I., Zabel, M., 2012a. Multiproxy characterization and budgeting of terrigenous end-members at the NW African continental margin. Geochem. Geophys. Geosyst. 13 (9)https://doi.org/10.1029/2012GC004148.

Just, J., Dekkers, M.J., Dobeneck, T., Hoesel, A., Bickert, T., 2012b. Signatures and significance of aeolian, fluvial, bacterial and diagenetic magnetic mineral fractions in Late Quaternary marine sediments off Gambia, NW Africa. Geochem. Geophys. Geosyst. 13 (9)https://doi.org/10.1029/2012GC004148.

Just, J., Schefuß, E., Kuhlmann, H., Stuut, J.B.W., Pätzold, J., 2014. Climate induced sub-basin source-area shifts of Zambezi River sediments over the past 17ka. Palaeogeogr. Palaeoclimatol. Palaeoecol. 410, 190–199. https://doi.org/10.1016/j.palaeo.2014.05.045.

King, E.L., 2012. Mineral resource assessment of the shallowest bedrock and overburden, Laurentian Channel, Newfoundland: potential marine protected area. Geol. Surv. Can. Open File 6969, 27. https://doi.org/10.4095/289847.

King, E.L., 2014. The Shallow Geology of a Portion of Laurentian Channel East of Cape Breton Island, Offshore Nova Scotia and Newfoundland and Labrador. Geological Survey of Canadahttps://doi.org/10.4095/293173, Open File 6731.

King, J., Banerjee, S.K., Marvin, J., Özdemir, , 1982. A comparison of different magnetic methods for determining the relative grain size of magnetite in natural materials: some results from lake sediments. Earth Planet. Sci. Lett. 59 (2), 404–419. https://doi.org/10.1016/0012-821X(82)90142-X.

Leng, W., von Dobeneck, T., Bergmann, F., Just, J., Mulitza, S., Chiessi, C.M., St-Onge, G., Piper, D.J.W., 2018. Sedimentary and rock magnetic signatures and event scenarios of deglacial outburst floods from the Laurentian Channel Ice Stream. Quat. Sci. Rev. 186, 27–46. https://doi.org/10.1016/j.quascirev.2018.01.016.

Löfberg, J., 2004. YALMIP: a toolbox for modeling and optimization in MATLAB. In: IEEE Internat. Sympos. Comput. Aided Control Systems Design (Taipei, Taiwan). pp. 284–289. https://doi.org/10.1109/CACSD.2004.1393890.

Loring, D.H., Nota, D.J.G., 1973. Morphology and sediments of the Gulf of St. Lawrence. Ottawa. Bull. Fish. Res. Board Can. 182, 147.

Lucchi, R.G., Sagnotti, L., Camerlenghi, A., Macrí, P., Rebesco, M., Pedrosa, M.T., Giorgetti, G., 2015. Marine sedimentary record of meltwater pulse 1a along the NW barents sea continental margin. Arktos 1 (7)https://doi.org/10.1007/s41063-015-0008-6.

Maher, B.A., 1988. The magnetic properties of some synthetic sub-micron magnetites. Geophys. J. R. Astron. Soc. 94, 83–96. https://doi.org/10.1111/j.1365-246X.1988.tb03429.x.

Margold, M., Stokes, C.R., Clark, C.D., 2018. Reconciling records of ice streaming and ice margin retreat to produce a palaeogeographic reconstruction of the deglaciation of the Laurentide Ice Sheet. Quat. Sci. Rev. 189, 1–30. https://doi.org/10.1016/j.quascirev.2018.03.013.

Mulitza, S., Bergmann, F., Brück, L., Chiessi, C.M., Govin, A., Klann, M., Kuhnert, H., Lübben, B., Max, L., Meyer, V., Morard, R., Müller, V., Patton, G., Paul, A., Poirier, A., Riesen, P., Schade, T., Stöber, U., Völker, G.S., Völpel, R., von Dobeneck, T., 2015. Cruise No. MSM39-June 07-June 25, 2014-St. John's, (Canada)-St. John's, (Canada). MARIA S. MERIAN-Berichte, MSM39. In: DFG-Senatskommission für Ozeanographie. p. 89. https://doi.org/10.2312/cr_msm39.

Needham, H.B., Habib, D., Heezen, B.C., 1969. Upper Carboniferous palynomorphs as a tracer of red sediment dispersal patterns in the northwest Atlantic. J. Geol. 77 (1), 113–120. https://doi.org/10.1086/627414.

Nesbitt, H.W., Young, G.M., McLennan, S.M., Keays, R.R., 1996. Effects of chemical weathering and sorting on the petrogenesis of siliciclastic sediments, with implications for provenance studies. J. Geol. 104 (5), 525–542. https://doi.org/10.1086/629850.

Pe-Piper, G., Triantafyllidis, S., Piper, D.J.W., 2008. Geochemical identification of clastic sediment provenance from known sources of similar geology: the Cretaceous Scotian Basin. Canada. J. Sediment. Res. 78 (9), 595–607. https://doi.org/10.2110/jsr.2008.067.

Piper, D.J.W., Slatt, R.M., 1977. Late Quaternary clay-mineral distribution on the eastern continental margin of Canada. Geol. Soc. Am. Bull. 88, 267–272. https://doi.org/10.1130/0016-7606(1977)88<267:LQCDOT>2.0.CO;2.

Piper, D.J.W., Macdonald, A., 2001. Timing and position of Late Wisconsinan ice-margins on the upper slope seaward of Laurentian Channel. Géogr. Phys. Quaternaire 55 (2), 131–140. https://doi.org/10.7202/008298ar.

Piper, D.J.W., Skene, K.I., 1998. Latest Pleistocene ice-rafting events on the Scotian Margin (eastern Canada) and their relationship to Heinrich events. Paleoceanography. 13(2), 205-214. doi:10.1029/97PA03641Piper, D.J.W., Shaw, J., Skene, K.I., 2007. Stratigraphic and sedimentological evidence for late Wisconsinan sub-glacial outburst floods to Laurentian Fan. Palaeogeogr. Palaeoclimatol. Palaeoecol. 246 (1), 101–119. https://doi.org/10.1016/j.palaeo.2006.10.029.

Piper, D.J.W., Deptuck, M.E., Mosher, D.C., Hughes Clarke, J.E., Migeon, S., 2012. Erosional and depositional features of glacial meltwater discharges on the eastern Canadian continental margin. SEPM (Soc. Sediment. Geol.) Spec. Publ. 99, 61–80, 978-1-56576-304-3.

Razik, S., Govin, A., Chiessi, C.M., von Dobeneck, T., 2015. Depositional provinces, dispersal, and origin of terrigenous sediments along the SE South American continental margin. Mar. Geol. 363, 261–272. https://doi.org/10.1016/j.margeo.2015.03.001.

Rémillard, A.M., St-Onge, G., Bernatchez, P., Hétu, B., Buylaert, J.-P., Murray, A.S., Lajeunesse, P., 2017. Relative sea-level changes and glacio-isostatic adjustment on the Magdalen Islands archipelago (Atlantic Canada) from MIS 5 to the late Holocene. Quat. Sci. Rev. 171, 216–233. https://doi.org/10.1016/j.quascirev.2017.07.015.

Roger, J., Saint-Ange, F., Lajeunesse, P., Duchesne, M.J., St-Onge, G., 2013. Late quaternary glacial history and meltwater discharges along the Northeastern Newfoundland shelf. Can. J. Earth Sci. 50 (12), 1178–1194. https://doi.org/10.1139/cjes-2013-0096.

Shaw, J., Piper, D.J.W., Fader, G.B.J., King, E.L., Todd, B.J., Bell, T., Batterson, M.J., Liverman, D.G.E., 2006. A conceptual model of the deglaciation of Atlantic Canada. Quat. Sci. Rev. 25 (17), 2059–2081. https://doi.org/10.1016/j.quascirev.2006.03.002.

Shaw, J., 2002. The meltwater hypothesis for subglacial bedforms. Quat. Int. 90 (1), 5–22. https://doi.org/10.1016/S1040-6182(01)00089-1.

Simon, Q., Hillaire-Marcel, C., St-Onge, G., Andrews, J.T., 2014. North-eastern Laurentide, western Greenland and southern Innuitian ice stream dynamics during the last glacial cycle. J. Quat. Sci. 29 (1), 14–26. https://doi.org/10.1002/jqs.2648.

Skene, K.I., Piper, D.J.W., 2003. Late Quaternary stratigraphy of Laurentian Fan: a record of events off the eastern Canadian continental margin during the last deglacial period. Quat. Int. 99, 135–152. https://doi.org/10.1016/S1040-6182(02)00116-7.

Stokes, C.R., Tarasov, L., Blomdin, R., Cronin, T.M., Fisher, T.G., Gyllencreutz, R., Hättestrand, C., Heyman, J., Hindmarsh, R.C.A., Hughes, A.L.C., Jakobsson, M., Kirchner, N., Livingstone, S.J., Margold, M., Murton, J.B., Noormets, R., Peltier, W.R., Peteet, D.M., Piper, D.J.W., Preusser, F., Renssen, H., Roberts, D.H., Roche, D.M., Saint-Ange, F., Stroeven, A.P., Teller, J.T., 2015. On the reconstruction of palaeo-ice sheets: recent advances and future challenges. Quat. Sci. Rev. 125, 15–49. https://doi.org/10.1016/j.quascirev.2015.07.016.

Stoner, J.S., Channell, J.E.T., Hillaire-Marcel, C., 1996. The magnetic signature of rapidly deposited detrital layers from the Deep Labrador Sea: relationship to North Atlantic Heinrich layers. Paleoceanography 11 (3), 309–325. https://doi.org/10.1029/96PA00583.

Stoner, J.S., Andrews, J.T., 1999. the North Atlantic as a quaternary magnetic archive. In: Maher, B.B., Thompson, R. (Eds.), Quaternary Climate, Environments and Magnetism. Cambridge Univ. Press, New York, pp. 49–80.

Syvitski, J., Praeg, D., 1989. Quaternary sedimentation in the St. Lawrence Estuary and adjoining areas, Eastern Canada: an overview based on high-resolution seismo-stratigraphy. Géogr. Phys. Quaternaire 43 (3), 291–310. https://doi.org/10.7202/032784ar.

Todd, B.J., 2016. The Laurentian Channel: a major cross-shelf trough in Atlantic Canada. In: In: Dowdeswell, J.A., Canals, M., Jakobsson, M., Todd, B.J., Dowdeswell, E.K., Hogan, K.A. (Eds.), 2016. Atlas of Submarine Glacial Landforms: Modern, Quaternary and Ancient, vol. 46, Geological Society, London, Memoirs, pp. 161–162. https://doi.org/10.1144/M46.124.

Tsikouras, B., Pe-Piper, G., Piper, D.J., Schaffer, M., 2011. Varietal heavy mineral analysis of sediment provenance, Lower Cretaceous Scotian Basin, eastern Canada. Sediment. Geol. 237 (3–4), 150–165. https://doi.org/10.1016/j.sedgeo.2011.02.011.

Vali, H., von Dobeneck, T., Amarantidis, G., Förster, O., Morteani, G., Bachmann, L., Petersen, N., 1989. Biogenic and lithogenic magnetic minerals in Atlantic and Pacific deep sea sediments and their paleomagnetic significance. Geol. Rundsch. 78 (3), 753–764. https://doi.org/10.1007/BF01829320.

Weltje, G.J., Tjallingii, R., 2008. Calibration of XRF core scanners for quantitative geochemical logging of sediment cores: theory and application. Earth Planet. Sci. Lett. 274 (3–4), 423–438. https://doi.org/10.1016/j.epsl.2008.07.054.

Weltje, G.J., 2012. Quantitative models of sediment generation and provenance: state of the art and future developments. Sediment. Geol. 280, 4–20. https://doi.org/10.1016/j.sedgeo.2012.03.010.

Wheeler, J.O., Hoffman, P.F., Card, D.K., Davidson, A., Sanford, B.V., Okulitch, A.V., Roest, W.R., 1996. Geological map of Canada. Geol. Surv. Can. Map 1860A Scale 1 (5)https://doi.org/10.4095/208175, 000,000.

Williams, H., Grant, A.C., 1998. Tectonic assemblages, Atlantic region, Canada. [1:3m map] geological survey of Canada. Open File 3657, https://doi.org/10.4095/209977.